Studies of growth of metal nanostructures on single crystal surfaces

A THESIS

submitted in partial fulfilment for the degree of

Master of Science

as part of the

Integrated Ph.D. programme

(Materials Science)

by

VARUN THAKUR

CHEMISTRY AND PHYSICS OF MATERIALS UNIT

JAWAHARLAL NEHRU CENTRE FOR ADVANCED SCIENTIFIC RESEARCH

BANGALORE, INDIA

March 2011

Studies of growth of metal nanostructures on single crystal surfaces

A THESIS

submitted in partial fulfilment for the degree of

Master of Science

as part of the

Integrated Ph.D. programme

(Materials Science)

by

VARUN THAKUR

CHEMISTRY AND PHYSICS OF MATERIALS UNIT

JAWAHARLAL NEHRU CENTRE FOR ADVANCED SCIENTIFIC RESEARCH

BANGALORE, INDIA

March 2011

Dedicated to

My mother

DECLARATION

I hereby declare that the matter embodied in the thesis entitled "**Study of growth of metal nanostructures on single crystal surfaces**" is the result of investigations carried out by me at the Chemistry and Physics of Materials Unit, Jawaharlal Nehru Centre for Advanced Scientific Research, India under the supervision of Prof. S. M. Shivaprasad and that it has not been submitted elsewhere for the award of any degree or diploma.

In keeping with the general practice in reporting the scientific observations, due acknowledgement has been made whenever the work described is based on the findings of other investigators. Any omission that might have occurred due to oversight or error in judgement is regretted.

Varun Thakur

CERTIFICATE

March 31, 2011

It is certified that the work described in this report "**Studies of growth of metal nanostructures on single crystal surfaces**" is a *bona fide* record of the research work carried out by Mr. Varun Thakur under my supervision in MBE (epitaxy) Lab, International Centre for Material Sciences (ICMS), Jawaharlal Nehru Centre for Advanced Scientific Research, Bangalore, India. The contents of this thesis have not been submitted any other university or institute for the award of any degree or diploma.

Supervisor signature

Bangalore 560 064

Professor S.M.Shivaprasad

CPMU & ICMS, JNCASR

ACKNOWLEDGEMENT

It is with a deep sense of gratitude that I thank my thesis supervisor, Prof. S.M.Shivaprasad, for providing me an opportunity to work on the wondrous field of surface physics. His acute sense of understanding and problem solving has always been a source of motivation for me. I shall be eternally grateful to him for giving me enough freedom to think on my own and be always there for me whenever I am faced with a problem.

I am also grateful to Prof. G.U.Kulkarni for advising me about the experimental part of my thesis. His ability to come up with wonderful ideas has been another source of encouragement for me. It has been an enriching experience for me of working with him.

My heartiest acknowledgements are towards Prof. Shobhana Narsimhan, who taught and advised me about the theoretical aspect of my work. The way she comes up with new ideas each time we discuss has always driven me to best myself everytime.

My labmates have been very helpful to me whenever I have required any sort of assistance, and for that I am humbly grateful to all of them, Praveen, Jithesh, Manoj, Satish, Malli, Darshana and Sreedhar.

I especially thank Jithesh for helping me out with the theoretical aspect of my work and for teaching me some nuances of surface science.

It was a pleasure working with K. Venu, with whom I started the experiments involving Ag on GaN. His methodical way of going about a job was a joy to watch.

The faculty of JNC, who have put in so much effort in their coursework, deserve a special mention in the acknowledgements. I am indebted to all of them for widening my

scientific knowledge through a vast range of courses. I thank Prof. G.U. Kulkarni, Prof. S. Balasubramanian, Prof. M. Eswaramoorthy, Dr. T.K. Maji, Prof. K.S. Narayan, Dr. A. Sundaresan, Prof. Chandrabhas Narayana, Dr. Ranjan Datta, Prof. Shobhana Narsimhan, Prof. U.V.Waghmare, Prof. S.K. Pati, Dr. N.S. Vidhyadhiraja and Prof. S. Ranganathan (Materials Engineering, IISc) for their coursework.

I thank all my batchmates of Int. Ph.D 2008, Arpan, Chidambar, Dileep, Gayatri, Pandu, Rana, Sharma and Sudeshna for their company and support during my MS programme.

I am also thankful to all the people who have helped me during the various measurements I have taken during this work: Vasu and Jithesh, for UV and PL studies, Malli and Kishore for XPS measurements, Anil and Nitesh for XRD, Manoj for HR-XRD, Mahesh for SEM, Selvi for FESEM, Basavaraju and Mallikarjun for AFM.

I acknowledge the help of Somasekar for PVD growth and Manoj and Satish for MBE growth.

Lastly, I would like to thank my parents for their support and for being there for me whenever I needed them. They are the ones who are responsible for moulding me into whatever I am today, and for that, I remain forever in their debt.

Table of Contents

Declaration i

Certificate ii

Acknowledgements iii

Preface vii

Synopsis xi

Abbreviations xiii

Part A

A.1 Introduction **1**

A.1.1 Surface Plasmons 1
A.1.1.1 coupling to surface plasmons 3
A.1.1.2 Propagation of surface plasmons on metal surfaces 4
A.1.1.3 Losses in surface plasmons 5

A.1.2 Gallium Nitride 6
A.1.2.1 Structure and Properties 8
A.1.2.2 c-plane Gallium Nitride 9
A.1.3 Motivation 11

A.2 Experimental **15**

A.2.1 Growth Techniques 15
A.2.1.1 Molecular Beam Epitaxy 15
A.2.1.2 Electroless Deposition 17
A.2.1.3 Physical Vapour Deposition 18

A.2.2 Characterization Techniques **22**
A.2.2.1 SEM 23
A.2.2.1.1 FESEM 24
A.2.2.2 EDX/Elemental Mapping 25
A.2.2.3 Photoluminescence 26
A.2.2.4 Absorption 27
A.2.2.4.1 Reflectance Measurement 27
A.2.2.5 XRD 28
A.2.2.5.1 HR-XRD 28
A.2.2.6 RHEED 29
A.2.2.7 XPS 30

A.2.2.8 AFM 32

A.3 Results **33**

A.3.1 Growth of GaN on c-plane sapphire 33

A.3.2 Properties of the GaN film 34

A.3.3 Deposition of Ag nanoparticles on GaN network 39
A.3.3.1 Chemical Route 40
A.3.3.2 Physical route 49
A.3.3.3 Flat GaN 55

A.3.4 Discussion 59

A.3.5 Conclusions 65

A.3.6 Extra work attempted 66

Part B

B.1 Introduction **67**

B.1.1 Epitaxial growth 68

B.1.2 Growth modes 69

B.1.3 CO-Nickel-Ruthenium system 71

B.2 Experimental Motivation **73**

B.2.1 Summary of the experiment 73

B.2.2 Results and discussion 73

B.2.3 Conclusions 78

B.3 Theoretical Studies **79**

B.3.1 Introduction 79

B.3.2 Results and Discussion 80

B.3.3 Conclusions 85

References **87**

PREFACE

From the 20th century onwards, nanomaterials have exceedingly become interesting topics of research due to their remarkable properties, which arise mainly due to their size. As one goes on decreasing the size of a particle, quantum effects begin to dominate and the physical and chemical properties change drastically. The physical and chemical properties of substances can be significantly altered when they are exhibited on a nanometre length scale, and this phenomenon opens up a completely new perspective for materials design that benefits from the introduction of not only particle size, but also particle morphology as new, powerful parameters. The unusual properties arise from the material dimensions that are of the order of the electron mean free path, which motivates their diverse application potential unexplored before.

Silver, gold and copper colloids have been the major focus of interest because of their unique optical properties determined by the collective oscillations of electron density, i.e. plasmons. Strong absorption in the near UV-visible range induces the brilliant colour of the metal nanoparticles in colloidal dispersion. It is produced by the strong coupling of nanoparticles to the electromagnetic radiation of incident light, leading to a collective excitation of all of the free electrons in the particles. Silver particles have the unique property that the excitation of the collective oscillation (plasmon absorption, λ = 380nm) and of the interband transitions (λ = 320nm) occur in separate wavelength regimes. The surface plasmon resonance should shift slightly to high energy, and broaden somewhat as the particle size is decreased. The intensity of absorption decreases remarkably until it is essentially unidentifiable for crystallites of less than 2nm effective diameter [1, 2].

Two of the most extensively studied systems are metal on semiconductor and metal on metal. The metal and semiconductor system studied in the present work consists of silver deposited on Gallium Nitride (GaN). The idea here is to modify the optical properties of GaN by introducing more states in the band gap region. The incentive for this work is based on the numerous findings of researchers related to surface plasmon coupling between metal nanoparticles and semiconductors band edge emission. In the present work, GaN nanowall-network structure formed by Molecular Beam Epitaxy (MBE) has been used as a substrate to grow silver particles. The silver has been deposited on GaN using a chemical (electroless deposition) as well as a physical route (e^--beam deposition). Various characterizations using sophisticated techniques such as SEM, FESEM, EDX etc. were performed on the samples. It was seen that there was noticeable difference between the samples grown by different routes. Moreover, to study the SPR coupling with GaN, the samples were annealed to different temperatures and the optical properties were studied. It was interesting to note that the photoluminescence spectra initially quenches with deposition of silver, but shows a strong enhancement as well as the emergence of new peaks with annealing. The enhancement may go up manifold, after which the spectrum again quenches. To explain these results, a model has been proposed, which is given in later chapters. The reason for why there is an enhancement of emission when the films are annealed is explained in terms of coupling between surface plasmons of silver and the excitons of GaN. The surface plasmon coupling between the silver particles and the semiconductor excitons give extra states in the band gap region of the GaN. This is because the resonance energy of silver on GaN interface (~2.9eV) is quite close to the band gap of GaN (3.3eV). There is an exchange of energy between the GaN and silver, which can lead to extra states arising in the band gap region of GaN.

In noble metals, such as silver in the present case, the decrease in size below the electron mean free path (the distance the electron travels between scattering oscillations with

the lattice centres) gives rise to intensive absorbance in the near UV – visible light. This results from the coherent oscillations of the free electron from one surface of the particle to the other, and is called the surface plasmon absorption. Researchers in high-vacuum surface science and electrochemistry fields have observed different catalytic efficiencies for the different metallic surfaces [3]. Atoms on different types of faces of a single metallic nanocrystal have different electronic structures, and thus promote different catalytic properties. The shift of the Fermi level manifests itself as a drastically increased sensitivity of the metal particles toward oxidation.

Another case of metal on metal growth is quite commonly studied these days. Different applications like catalysis and device manufacture require knowledge of how one material grows over the other. However, theoretical analyses of many of the experimental results are unknown. In order to get a more in-depth understanding of such systems, it is very important to compliment it with a good theoretical study done on them. In the work described in this thesis, an attempt has been made to theoretically explain the experimental results of the growth of nickel on ruthenium. The experiment shows the growth of nickel on ruthenium in the presence of CO. Nickel grows on ruthenium in forms of islands, and in the presence of CO, a particular type of island (quartet reconstructed) is preferentially formed. Many ideas have been proposed in the experiment, but an experimental validation is still needed for understanding exactly the mechanism behind these processes.

In the theoretical studies, density functional theory has been employed as a theoretical tool. Basic studies such as on which site the nickel sits on ruthenium, hcp or fcc, have been the starting points in the calculations. More complex structures have been examined later, to study the pseudomorphic growth of nickel on ruthenium, including a change in lattice constant to deliberately make the nickel sit in a strained way. Also, many of the suggestions coming from experimental observations have been tried, including the quartet reconstruction

and the influence of CO absorption. The results obtained from the ensuing theoretical studies are presented, and are shown to deviate from the experimental observations.

Synopsis

This thesis consists of two research problems, both involving metal nanoparticles deposited on single crystal surfaces. There is one experimental and one theoretical study shown. In the first part, which is experimental, the study is done on a metal-semiconductor interface. The theoretical study is motivated by an experiment, where metal nanostructures were grown on a single crystal metallic surface.

The first problem involved the growth of silver nanoparticles on c-plane gallium nitride surface. This problem investigates the kind of interactions existing between metal nanoparticles and a semiconducting surface. Although such kind of problems have been dealt with in the past, with many semiconducting quantum wells being regular templates to study such kind of processes, this study is done on just one semiconducting surface. The idea here is to know whether the processes described in various publications are limited to the presence of a quantum well or is it possible to study the same on just one semiconductor.

Part A

Chapter A.1 introduces the basic idea of optical properties of group III semiconductors, before explaining about surface plasmons and the various processes associated with them. In the end, GaN is introduced, with basic properties and growth methods discussed.

Chapter A.2 provides a short description of the characterization techniques used in this problem.

Chapter A.3 discusses the studies done in this problem, with all the results and inferences given. Conclusions are then made and a few ideas for future studies are presented.

The second problem is a theoretical study of the growth of nickel islands growing on a single crystal ruthenium (0001) surface in the presence of CO as a surfactant. Density functional theory (DFT) was used as a tool for this study. This work has been motivated by an experiment, which is also summarized in this thesis.

Part B

Chapter B.1 introduces the basic idea of this problem, which is to study the reactivity of transition metal surfaces. Different types of growth modes associated with thin films are also summarized.

Chapter B.2 summarizes the experiment which was the motivation behind this study. The important results are discussed and some intuitive ideas that were presented in context with this experiment are also given.

Chapter B.3 discusses the various results and inferences obtained in the theoretical studies done. In the end, conclusions have been made about this study.

References

ACRONYMS

1D/2D/3D	One-Dimensional/Two-Dimensional/Three-Dimensional
AES	Auger Electron Spectroscopy
AFM	Atomic Force Microscopy
CL	Cathodoluminescence
CVD	Chemical Vapor Deposition
DFT	Density Functional Theory
ESCA	Electron Spectroscopy for Chemical Analysis
FESEM	Field Emission Scanning Electron Microscopy
FM	Frank van-der Merwe (growth mode)
HRXRD	High Resolution X-ray Diffraction
LED	Light Emitting Diode
MBE	Molecular Beam Epitaxy
MOCVD	Metal Organic Vapor Phase Epitaxy
PES	Photoelectron Spectroscopy
PVD	Physical Vapor Deposition
PL	Photoluminescence
RHEED	Reflection High Energy Electron Diffraction
SEM	Scanning Electron Microscopy
SK	Stranski-Krastonov (growth mode)
UHV	Ultra High Vacuum
VW	Volmer- Weber (growth mode)
XPS	X-ray Photoelectron Spectroscopy
XRD	X-ray Diffraction

PART A

Modifying optical properties of Gallium Nitride nanowall network by silver nanoparticles deposition

Chapter A.1

Introduction

The need to attain energy security has prompted intense research in the fields of solid state lighting and full spectrum solar cells. In addition to conventional systems, wide band gap semiconductors are explored for their great potential via band gap engineering, where different regions are suitably alloyed to have a different band gap, so that the device can cover the entire visible range and also in the IR and UV. However, controlling defects, interface properties, morphology and inherent strain are challenges that need to be overcome to improve the luminous efficiencies of these optoelectronic devices.

Recently, the focus has been on metal or surface plasmon induced local field enhancements [4, 5]. It is believed that as the surface plasmon energy of the metals matches with the emitted photon energy of the surrounding materials, the resulting resonance can lead to an energy transfer from the metal surface to the surrounding or vice-versa [6, 7].

A.1.1 Surface Plasmons

Surface plasmons (SPs) are of interest to a wide spectrum of scientists, ranging from physicists, chemists and material scientists to biologists. Renewed interest in SPs comes from recent advances that allow metals to be structured and characterized on the nanometer scale. This in turn has enabled us to control SP properties to reveal new aspects of their underlying science and to tailor them for specific applications. For instance, SPs are being

explored for their potential in optics, magneto-optic data storage, microscopy and solar cells, as well as being used to construct sensors for detecting biologically interesting molecules. SPs were widely recognized in the field of surface science following the pioneering work of Ritchie in the 1950s [8]. SPs are waves that propagate along the surface of a conductor, usually a metal. These are essentially light waves that are trapped on the surface because of their interaction with the free electrons of the conductor (strictly speaking, they should be called surface plasmon polaritons to reflect this hybrid nature [9]). In this interaction, the free electrons respond collectively by oscillating in resonance with the light wave. The resonant interaction between the surface charge oscillation and electromagnetic field of the light constitutes the SP and gives rise to its unique properties.

For researchers in the field of optics, one of the most attractive aspects of SPs is the way in which they help us to concentrate and channel light using sub-wavelength structures. This could lead to miniaturized photonic circuits with length scales much smaller than those currently achieved [10, 11]. Such a circuit would first convert light into SPs, which would then propagate and be processed by logic elements, before being converted back into light, To build such a circuit one would require a variety of components: waveguides, switches, couplers and so on. Currently much effort is being devoted to developing such SP devices; one example is the 40 nm thick gold stripe that acts as a waveguide for SPs (Fig.1). An appealing feature is that, when embedded in dielectric materials, the circuitry used to propagate SPs can also be used to carry electrical signals. Developments such as this raise the prospect of a new branch of photonics using SPs, sometimes called plasmonics. The use of SPs to help us concentrate light in subwavelength structures stems from the different (relative) permittivities, ε, of the metals and the surrounding media. (ε is the square of the complex index of refraction). Concentrating light in this way leads to an electric field enhancement that can be used to manipulate light-matter

interactions and boost non-linear phenomena. For example, metallic structures much smaller than the wavelength of light are vital for the massive signal enhancement achieved in surface-enhanced Raman spectroscopy (SERS) – a technique that can now detect a single molecule [12, 13]. Furthermore, the enhanced field associated with SPs makes them suitable for use as sensors, and commercial systems have already been developed for sensing biomolecules.

A.1.1.1 Coupling to surface plasmons

The interaction between the surface charges and the electromagnetic field that constitutes the SP has two consequences. First, the interaction between the surface charge density and the electromagnetic field results in the momentum of the SP mode, $\hbar\boldsymbol{k}_{SP}$, being greater than that of a free-space photon of the same frequency, $\hbar\boldsymbol{k}_{0.}$($\boldsymbol{k}_0 = \omega/c$ is the free-space wavevector.) Solving Maxwell's equations under the appropriate boundary conditions yields the SP dispersion relation [55], that is, the frequency-dependent SP wavevector, $\boldsymbol{k}_{SP.}$

$$k_{SP} = k_0 \sqrt{\frac{\varepsilon_d \varepsilon_m}{\varepsilon_d + \varepsilon_m}} \qquad (1)$$

The frequency-dependent permittivity of the metal, ε_m and the dielectric material, ε_d, must have opposite signs if SPs are to be possible at such an interface. This condition is satisfied for metals because ε_m is both negative and complex (the latter corresponding to absorption in the metal). As an example, using equation (1), the SP wavevector for a silver-air interface in the red part of the visible part of the spectrum is found to be $\boldsymbol{k}_{SP} \approx 1.03.\boldsymbol{k}_0$. This increase in momentum is associated with the binding of the

SP to the surface, and the resulting momentum mismatch between light and SPs of the same frequency must be bridged if light is to be used to generate SPs.

The second consequence of the interaction between the surface charges and the electromagnetic field is that, in contrast to the propagating nature of SPs along the surface, the field perpendicular to the surface decays exponentially with distance from the surface. The field in this perpendicular direction is said to be evanescent or near field in nature and is a consequence of the bound, non-radiative nature of SPs, which prevents power from propagating away from the surface.

A.1.1.2 Propagation of surface plasmons on metal surfaces

Once light has been converted into an SP mode on a flat metal surface it will propagate but will gradually attenuate owing to losses arising from absorption in the metal. This attenuation depends on the dielectric function of the metal at the oscillation frequency of the SP. The propagation length, δ_{SP}, can be found by seeking the imaginary part, $\boldsymbol{k}''_{SP}$, of the complex surface plasmon wavevector, $\boldsymbol{k}_{SP} = \boldsymbol{k}'_{SP} + i\boldsymbol{k}''_{SP}$, from the SP dispersion equation (1),

$$\delta_{SP} = \frac{1}{2k''_{SP}} = \frac{c}{\omega}\left\{\frac{\varepsilon'_m + \varepsilon_d}{\varepsilon'_m \varepsilon_d}\right\}^{\frac{3}{2}} \frac{(\varepsilon'_m)^2}{\varepsilon''_m} \qquad (2)$$

where ε'_m and ε''_m are the real and imaginary parts of the dielectric functions of the metal, that is, $\varepsilon_m = \varepsilon'_m + i\varepsilon''_m$. Silver is the metal with the lowest losses in the visible spectrum; propagation distances are typically in the range 10-100μm, increasing towards 1mm as one moves into the 1.5 μm near-infrared telecom band. In the past, absorption by the metal was seen as such a significant problem that SPs were not considered viable for photonic

elements; the SP propagation length was smaller than the size of components at that time. This view is now changing due to recent demonstrations of SP-based components that are significantly smaller than the propagation length [14]. Such developments open the way to integrate many SP-based devices into circuits before propagation losses become too significant.

A.1.1.3 Losses in surface plasmons

In addition to dealing with the problem of loss owing to absorption in the metal, there is another key loss mechanism that must be considered: unwanted coupling to radiation. To build SP-based circuits one will need components that convert one SP mode into another, for example, a switch to re-route SPs without scattering the SP mode in such a way as to lose its energy to freely propagating light.

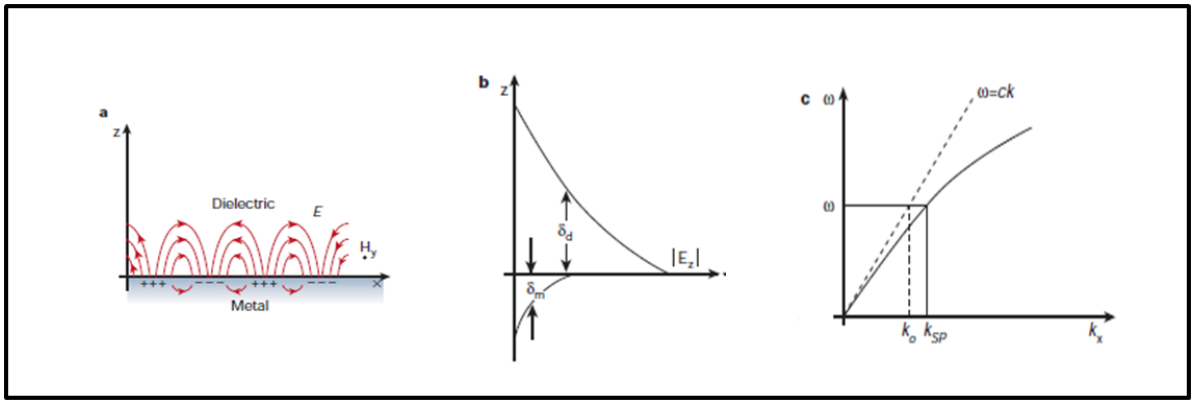

Fig.1 **(a)** *Transverse magnetic character of SP waves.* **(b)** *ω v/s k diagram for surface plasmons* **(c)***The dispersion curve for a SP mode*

The transverse magnetic character of SP waves is shown (Fig.1 (a)). The generation of electric charge acquires an electric field normal to the surface. This combined factor also leads to the field component perpendicular to the surface being enhanced near the surface and decaying exponentially with distance away from it. (b) The graphs between ω and k show this same evanescent nature of the electromagnetic field, reflecting the bound, non-

propagating nature of the surface plasmons. This prevents the power from escaping the surface. In the dielectric medium above the metal, typically air or glass, the decay length of the field, δ_d, is of the order of half the wavelength of light involved, whereas the decay length into the metal, δ_m, is determined by the skin depth. (c) The momentum mismatch problem that must be overcome in order to couple light and SP modes together is shown, with the SP mode always lying beyond the light line; that is,it has greater momentum ($\hbar k_{SP}$) than a free space photon ($\hbar k_0$) of the same frequency ω.

In particular, the collective oscillations of electrons in noble metal nanoparticles embedded in a dielectric matrix are localized surface plasmons (LSPs). The resonant excitation of LSPs leads to selective photon absorption and enhancement of local electromagnetic fields near the metal nanoparticles by orders of magnitude.

A.1.2 Gallium Nitride

Gallium Nitride (GaN), a key member of the group III nitride family, was synthesized almost 70 years ago (1938) by Juza and Hahn [15] by passing ammonia over hot gallium. However, much later intense interest in the material is due to the group of scientists gathered around Jacques Pankove at RCA. At this moment the scientific community began to fully realize the importance of semiconductors for the construction of a new type of light emitters: semiconductor light emitting-diodes (LEDs) and laser diodes (LDs). Gallium nitride together with AlN and InN form a group of materials characterized by a direct band gap of a value covering a huge spectral range: 0.7-6.2 eV. Thus, these semiconductors could potentially become a base for short-wavelength light emitter production. However, all these materials are difficult to grow and to dope [16]. In the 1970s, GaN was grown by the HVPE (hydride vapour phase epitaxy) method on sapphire. The

quality and purity of these layers were very poor, not allowing realization of more complicated structures or devices [17]. It was not possible to fabricate GaN p-n junction at that time, and this was the main reason why nitride activity lost its momentum.

20 years later Japanese researchers developed the epitaxial growth method which opened a new path for the synthesis of thin layers of GaN, InGaN, and AlGaN by MOVPE (metal organic vapour phase epitaxy). The problem of large lattice mismatch between gallium nitride and the most commonly used substrate (sapphire) was overcome through the application of a low-temperature nucleation layer [18]. It helped reduce the number of dislocations and maintain two-dimensional growth of nitride epilayers. Moreover, the discovery of p-type conductivity in GaN:Mg by Amano and Akasaki [19] in 1989 removed the last barrier for the construction of optoelectronic devices based on Group III nitrides. The final step in the demonstration of real nitride devices was made by Shuji Nakamura, a Japanese researcher from Nichia Chemical [20] who put blue and green LEDs into the world market.

Since the early work on nitride semiconductors, an important issue has been a choice of the proper (lattice and thermal expansion matched) substrate. The most commonly used substrate, sapphire, does not fulfil these requirements. Epistructures grown on sapphire contain typically 10^8-10^9 dislocations per square centimeter. Gallium nitride crystal is an ideal substrate for the growth of high-quality epitaxial layers of gallium nitride and InGaN/AlGaN with low content of In and Al. However, the single crystals of GaN are available only in small quantities, and they usually have small dimensions, limiting their use in large-scale production. A similar situation is the case of single crystals of AlN. Much effort has been devoted to developing low-dislocation GaN structures that could be used as a substrate for further epitaxy.

A.1.2.1 Structure and Properties:

Lattice parameters for ideal GaN, InN and AlN

AlN, GaN and InN crystallize in the wurtzite structure (space group C^4_{6v} –PC_6mc), which is characterized by lattice parameters *a* and *c*, as well as by *u*-value (*u* = *b*/*c*, where *b* is a bond length in the *c* direction). For the ideal wurtzite structure, *c*/*a* = 1.633 and *u* = 0.375. The structure parameters for the III nitride are given in Table 1. For GaN, the wurtzite structure is nearly ideal, and all four Ga-N distances have almost equal bond lengths, and the bond angles agree with the values for a regular tetrahedron. AlN deviates significantly from the ideal parameters. Its interatomic distances and bond angles differ by 0.01Å and 3°, respectively. The deviations from the ideal wurtzite structure have an important impact on the spontaneous polarization of the nitride.

The cubic zinc blende phase of GaN (space group of T^2_d-F43m and lattice parameter of about 4.5 Å) is a metastable one and observed only for heteroepitaxial layers on highly mismatched cubic (001)-oriented substrates, for example, on GaAs [21] or Si [22].

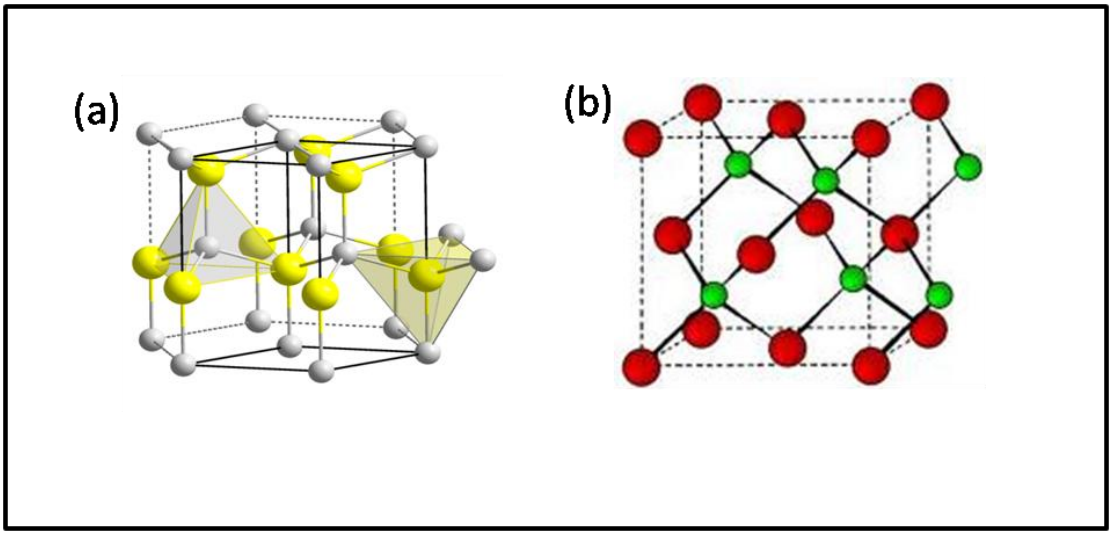

Fig.2 *(a) Wurtzite structure (b) zinc blende structure*

The other GaN metastable cubic rock salt phase (octahedrally coordinated) with a lattice parameter of 4.07 Å has been found for nanosize particles [23] and small precipitates in epilayers on sapphire [24]. This phase becomes stable at pressures above 40 GPa [25].

Compound	a(Å)	c(Å)	c/a	u	Ref.
AlN	3.1106	4.9795	1.601	0.382	[68]
GaN	3.1885	5.1850	1.627	0.377	[69, 70]
InN	3.5380	5.7030	1.612	No data	[71]

Table 1*. Lattice parameters of nitride semiconductors*

A.1.2.2 c-plane gallium nitride

The substrate requirements of GaN have previously been mentioned. For sapphire, the most common substrate, the lattice mismatch with GaN is ~ 33%, but if the substrate is

rotated with respect to the GaN, the lattice mismatch is reduced to ~16 %. The reduced numbers of dislocations make it easier to then grow a flatter film.

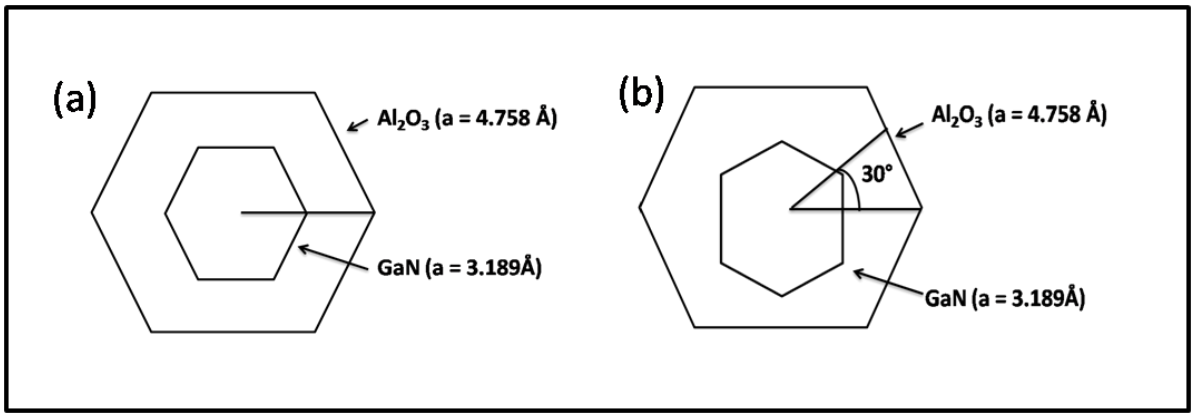

Fig.4 *(a) GaN on sapphire – on top configuration, (b) GaN on sapphire - 30° rotated*

Calculation of lattice mismatch:

(a) For the first case, lattice mismatch is calculated simply by subtracting the lattice parameters and dividing with the lattice parameter of the substrate:

$$\frac{3.189 - 4.758}{4.758} = -0.33 \text{ or } -33\%$$

The negative sign indicates a tensile stress, since the lattice parameter of GaN is lesser than that of Al_2O_3.

(b) In the second case, when the substrate is rotated by 30° relative to the GaN growth direction, the lattice mismatch is obtained by taking the projection of the GaN lattice parameter, which is now rotated by 30°, in the direction of the lattice parameter of Al_2O_3:

$$\frac{2 \times 3.189 \cos 30° - 4.758}{4.758} = +0.16 \text{ or } 16\%$$

Now, the sign of the mismatch changes to positive, since we take two unit cells of GaN to get the correct mismatch indicating that the stress is reversed to compressive upon a 30° rotation of the substrate.

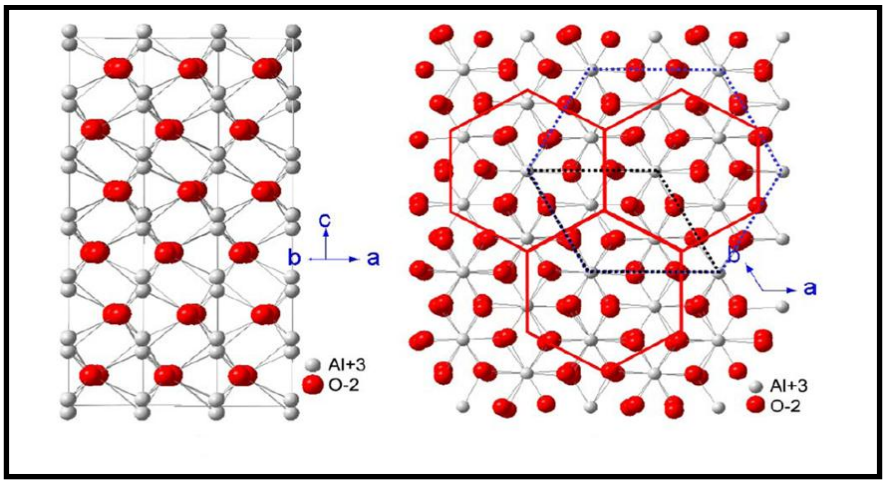

Fig.5 *(a) Atomic structure of sapphire (// c-axis); (b) atomic structure of sapphire (⊥ c-axis) and schematic illustration of the epitaxial relationship between (0001) GaN and c-sapphire. The dotted lines show the unit cells of sapphire while the solid lines show the unit cells of GaN*

Compound	**$[11\underline{2}0]_{III\text{-}N}$ || $[11\underline{2}0]_{sapphire}$**	**$[10\underline{1}0]_{III\text{-}N}$ || $[11\underline{2}0]_{sapphire}$**
AlN	-34.6%	+13.3%
GaN	-33.0%	+16.0%
InN	-25.4%	+29.2%

Table 2*. Lattice mismatches of III-N compounds with respect to sapphire is shown – the effect of rotation of substrate can also be observed [76]*

A.1.3 Motivation

The present work was motivated by reports of enhancement of emission of various semiconductors by metal nanoparticles [26-30]. Group III nitrides, such as GaN, InN, AlN and their alloys have been demonstrated as materials for high efficiency light emitting diodes [31-34], among other applications such as solar cells, lasers etc [35-37]. Although III-nitride based LEDs are already commercially available, further improvements in optical output power and external quantum efficiency (η_{ext}) are required [38]. The limited external quantum efficiency of LEDs is mainly attributed to limited internal quantum efficiency (η_{int}). The η_{int} is strongly influenced by non-radiative recombination processes of threading dislocations [39] and also by a separation of the electron and hole wavefunctions by the polarization-induced electric field [40, 41].

Recently, among many approaches for the improvement of η_{int}, surface plasmons have been actively studied to enhance the luminescence efficiency of light emitting materials and devices [7, 27-30, 42-44]. In particular, the collective oscillations of electrons in noble metal nanoparticles embedded in a dielectric matrix are localized surface plasmons (LSPs). The resonant excitation of LSPs leads to selective photon absorption and enhancement of local electromagnetic fields near the metal nanoparticles by orders of magnitude. The enhancement of local electromagnetic fields is strongly dependent on the distance between the quantum well (QW) and the metal nanoparticles. The penetration depth of the SP fringing field into the semiconductor is given by $Z = \lambda/2\pi[(\varepsilon'_{GaN} - \varepsilon'_{metal})/\varepsilon'^{2}_{GaN}]^{1/2}$, where ε'_{GaN} and ε'_{metal} are the real part of the dielectric constants of the semiconductor and the metal. The penetration depth is estimated to be 41nm for QW-SP coupling at an emission energy of 2.75eV (450nm) for a blue LED when using the real part of the dielectric constant of the GaN and Ag metal [29, 42]. Therefore, when the QW is located close to the Ag nanoparticles within a distance of 41nm, a strong resonant coupling between

the QW and the LSPs is expected to take place. Kwon *et al.* reported on the SP-enhanced LEDs using Ag nanoparticles which were inserted in the n-GaN layer underneath the multiple quantum wells (MQWs) [42]. However, it is difficult to control the distance between the Ag nanoparticles and the MQWs. In addition, a large amount of Ag nanoparticles is evaporated at a high growth temperature for the overgrown n-GaN capping layer and the crystal quality of InGaN QWs is also deteriorated by Ag nanoparticles embedded in n-GaN.

Recent approach has been to form nanostructures of GaN on sapphire that are defect free and can act as good transporters of electrons and photons. In this direction, we have formed GaN nanowall network that is wurtzite and c-oriented, with a large surface area. So we felt it would be interesting to study the adsorption of Ag nanoparticles on this strain relaxed surfaces, and try to measure the coupling between the band edge emission of GaN and the surface plasmons of Ag nanoparticles. The coupling is expected to enhance light emission, while the interface states can influence the frequency of emitted light.

Chapter A.2

Experimental

The experiments involved in this work consist of growth of GaN nanowall network and Ag nanoparticles, followed by characterization by several sophisticated probes. Below are present brief descriptions of the growth and characterization techniques used in the present study.

A.2.1 Growth techniques:-

A.2.1.1 Molecular Beam Epitaxy

MBE uses ultralow pressure (about 10^{-11} Torr before and 10^{-5} Torr N_2 partial pressure during the growth) and elemental sources of Ga, Al, In, Mg and Si. These elements are evaporated by heating them in separate quasi-Knudsen effusion cells. They get condensed onto the wafer held at the required temperature where they may react with each other to give a single-crystal compound as the product. The term "beam" means that the evaporated atoms do not interact with each other or the vacuum chamber, due to the long mean-free path of the atoms. Atomic nitrogen is obtained either from ammonia [72] or from nitrogen plasma generated by radio frequency (RF) [73] or cyclotron resonance sources [74]. The ammonia source has a big disadvantage of low cracking efficiency at low temperatures, and it is much more technically troublesome. Therefore, RF plasma is becoming the dominating technique, enabling the growers to achieve high growth rates

(up to almost 1μm/h for GaN) and very high-quality layers. However, the most important aspect of MBE has been the slow deposition rate (usually < 100 nm/h) which enables the films to grow epitaxially. The slow deposition rates require better vacuum than other deposition techniques, which is why the operating conditions of an MBE is ultra-high vacuum (UHV).

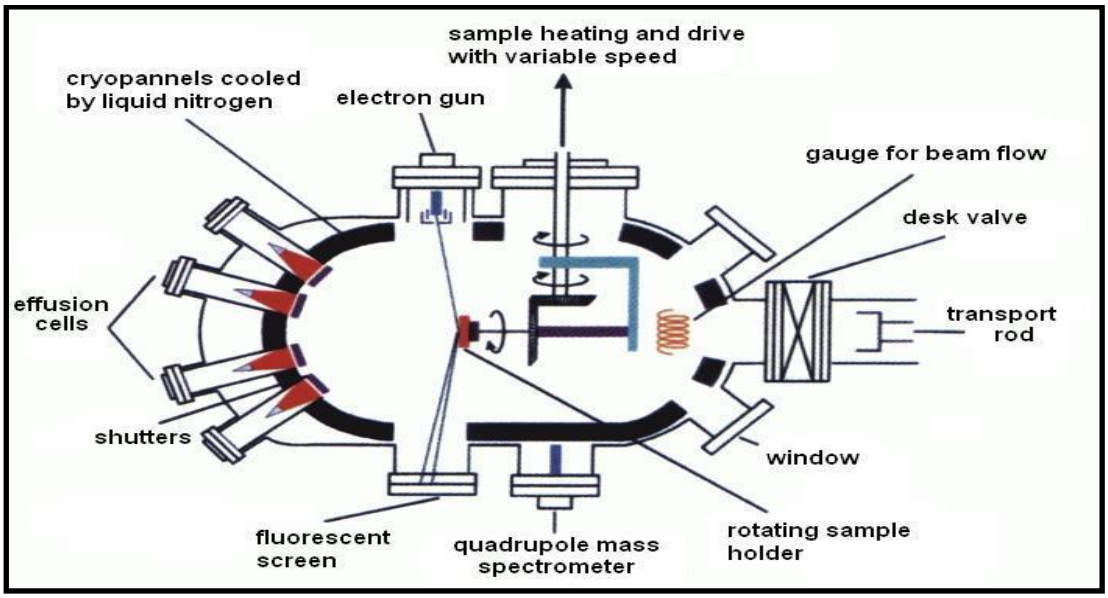

Fig.1 *Schematic diagram of a molecular beam epitaxy system – growth chamber shown*

Despite the fact that all commercial group III-nitride based optoelectronic devices are produced using the MOVPE technique, MBE is gaining increasing attention among nitride technologists. MOVPE has a big advantage of growing low-temperature buffer layers and thus growing GaN templates on foreign substrates. Because such MOVPE templates as well as free-standing GaN are commercially available, MBE has a chance to produce some devices with quality superior to MOVPE. Until now, all records of 2D electron-gas mobility at the AlGaN/GaN interface belong to MBE-grown samples [75]. Moreover, as the MBE growth process is conducted at low temperatures (in contrast to MOVPE, which must employ high temperatures to crack ammonia), the interfaces

between the QWs and barriers can be much sharper, which is crucial for LD operation. An additional advantage of the MBE process is that the p-GaN films are not passivated due to the absence of atomic hydrogen species during the growth. Another great advantage of using MBE is that we can have several characterization probes such as RHEED, CL, atomic absorption, mass spectroscopy, ellipsometry etc. in-situ during growth monitoring, which are very useful to understand the growth modes and mechanisms.

Fig.2 *MBE system used in the present study – purchased from SVT associates, USA*

A.2.1.2 Electroless Deposition:

Metallization of surfaces can be done in a number of ways, including vacuum evaporation deposition sputtering, electrochemical, and electroless deposition methods

[96-98]. Methods like sputtering present good alternatives for metallization of planar materials, but they are ineffective when plating materials that are rough or of high surface area, resulting in non-uniform metal coverage on the desired surface. Electrochemical deposition offers the advantage of working in solution and being cheaper and easier to do on a large scale than vacuum methods. However, the electrochemical approaches are affected by IR drops, mass transport, and overall conductivity of the material to be plated, since electrical contacts need to be made. Electrochemical plating also shows limitations for high surface area materials, being transport limited on high aspect ratio surfaces.

Electroless methods are less prone to such limitations. Electroless deposition generally refers to one of the two different processes: (1) direct electroless deposition, in which the metal is directly reduced by a reducing agent, or (2) a displacement reaction, in which a more active metal carries the reduction [99,100]. Both methods have been carefully studied in terms of their role in the deposition of metals on active and non-active surfaces, in getting smooth coatings or granular, catalytic coatings. One of the main challenges for such electroless methods has been that of effectively coating non-conducting or semiconducting surfaces. While most metals coat conducting films by direct electroless reduction, semiconducting or insulating films usually require the presence of an activator metal and are more akin to the displacement reaction, rendering it more commonly used for the plating of semiconducting or non-conducting materials.

A.2.1.3 Physical Vapour Deposition:

Industrial coating techniques can be broadly classified into three groups: Physical Vapour Deposition (PVD), Chemical Vapour Deposition (CVD), and spray processes. Each process can again be sub-classified based on the source of energy used

for the deposition of coatings as shown in Table 1. Each of these processes has advantages and disadvantages: chemical and physical conditions during the deposition reaction can strongly affect the composition, residual stresses, and microstructure (i.e. amorphous, polycrystalline, epitaxial, and textured) of the product. The effect of these conditions must be understood to control the process. Coating thickness, desired properties (including microstructure, physical, and mechanical properties), and the application will determine the coating process to be used.

Spray Deposition processes	Thermal spray High-velocity-oxy-fuel (HVOF) Detonation gun (D-gun)
Chemical Vapour Deposition processes (CVD)	Low pressure CVD Plasma enhanced CVD Photochemical and laser-CVD
Physical Vapour Deposition processes (PVD)	Thermal evaporation Electron beam evaporation Sputtering -Balanced and unbalanced magnetron sputtering -Direct current diode sputtering -Radio frequency sputtering -Triode-assisted PVD Ion plating and ion implantation

Table 1: *List of deposition techniques commonly used*

Some of the shortcomings of the CVD process can be addressed by the physical vapour deposition (PVD) process. The term PVD denotes those vacuum deposition processes where the coating material is evaporated by various mechanisms (resistance heating, high-energy ionized gas bombardment, or electron gun) under vacuum, and the vapour phase is transported to the substrate, forming a coating. PVD is a line-of-sight process in which atoms travel from the source material to the substrate in a straight path. The PVD coating process takes place between temperatures of 100-600°C. Sputtering is

one of the most versatile PVD processes available for thin film preparation. Various metallic and ceramic (carbides and nitrides) coatings can be applied by this process typically at a rate of a few μm or less per hour. Unlike CVD process, PVD processes are clean and pollution free. The main disadvantages of PVD processes (with the exception of EB-PVD) are the low deposition rates (1-5pm per hour) and the difficulty in applying oxide coatings efficiently.

The EB-PVD process: EB-PVD is a derivative of the electron beam melting technique. The first U.S. patent was issued to M.von Pirani in EB melting and refining of materials in March 1907. Perhaps the most consequential growth phase in EB technology began in the early 80s and is still in progress. The significant progress was driven by three factors: (1) much improved vacuum generation technology, (2) significant advances in computers, and (3) availability of high-quality EB guns. Since then, EB coating technology is constantly gaining reputation and confidence in a wide range of applications including thermal barrier ceramic coatings and wear-resistant hard coatings.

It has overcome some of the difficulties associated with the CVD, PVD, and metal spray processes. In the EB-PVD process, focused high-energy electron beams generated from electron guns are directed to melt and evaporate the target, and can also be used to preheat the substrate inside the vacuum chamber (Fig. 15). A wide variety of materials including refractory metals (such as tungsten), low vapour pressure metals (such as platinum), and alloys can be evaporated. Since the electron beam method concentrates large amounts of heat on a very small area, high rates of deposition are possible, a factor which is of interest to any production-oriented shop.

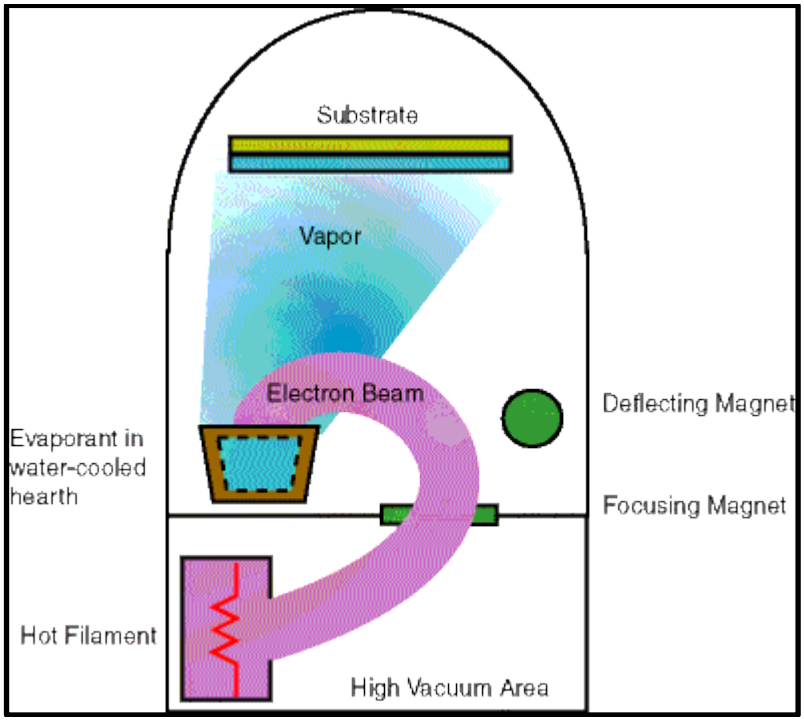

Fig.3 *An electron beam PVD setup: 1. Filament is heated until it emits electrons. 2. Electrons leave the gun. 3. The beam is focused and bent by the magnet. 4. The beam plays upon the surface of the evaporant causing heat and vaporization. 5. The vapour condenses on the substrate surface.*

Working Principle: The process begins under a vacuum of 10^{-5} Torr or less. A tungsten filament inside the electron beam gun is heated. The gun assembly is located outside the evaporation zone to avoid becoming contaminated by evaporant. When the filament becomes hot enough, it begins to emit electrons. These electrons form a beam which is deflected and accelerated toward and focused on the material to be evaporated by means of magnetic or electric fields. When the electron beam strikes the target surface, the kinetic energy of motion is transformed by the impact into thermal energy (heat). It is important to remember that the energy given off by a single electron is quite small and that the heating is accomplished simply by virtue of the vast number of electrons hitting the evaporant surface. This is the energy which vaporizes the target material. The energy level achieved in this manner is quite high – often more than several million watts per square inch. Due to the intensity of the heat generated by the electron

beam, the evaporant holder must be water cooled to prevent it from melting. The power supply for this operation is a high voltage D.C. power supply. The voltage is typically 10 to 30 kilovolts, with wattage ranging anywhere from 10 to 30 kilowatts.

Fig.4 *PVD system used in this study- purchased from SVT associates, USA*

A.2.2 Characterization Techniques:-

The different characterization techniques used in this work are mentioned below:

1. SEM /FESEM
2. EDX/Elemental Mapping
3. Photoluminescence
4. Absorption
5. XRD/HR-XRD
6. RHEED

7. XPS
8. AFM

A.2.2.1 SEM: The Scanning Electron Microscope (SEM) is a type of electron microscope that images a sample by scanning it with a high-energy electron beam. The scan pattern is raster type, meaning that the beam sweeps horizontally left to right and keeps moving one step down after each scan. The electrons interact with the sample atoms which gives information about the topography, composition and many other properties such as electrical conductivity.

Working principle: An electron beam is thermionically emitted from an electron gun which is fitted with a tungsten filament as a cathode. There are other cathodes also available, such as lanthanum hexaboride (LaB_6), but tungsten is more commonly used because of its low cost, high melting point and low vapour pressure, the latter two properties enabling the electron emission to occur. The electron beams have energies between 0.5 to 40 keV, and are focused using two condenser lenses to a spot 0.4-5 nm in diameter. The beam passes through the scanning coils, which deflect the beam in x and y directions in order to get the raster effect during scanning. There are various types of electronic amplifiers which are used to amplify the signals which are displayed as variations in brightness on a cathode ray tube. The resultant image is a distribution of intensity of the signal being emitted from the scanned area of the specimen. The image is captured digitally and viewed on a computer screen.

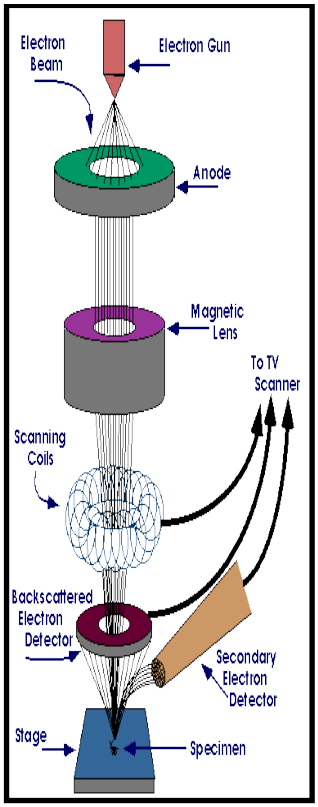

Fig.5 *Schematic diagram of a scanning electron microscope*

A.2.2.1.1 <u>FESEM:</u> A variant of SEM is the FESEM, which is Field-Emission SEM. The difference between the two techniques is only the addition of a field-emission cathode in the electron gun of a SEM. The main advantage of FESEM over conventional SEM is the improved spatial resolution, going down to 1.5 nm, which is 3 to 6 times better than SEM. It also does lesser damage to the sample as charging effects are reduced. The field-emission cathode provides narrower probing beams at low as well as high electron energy.

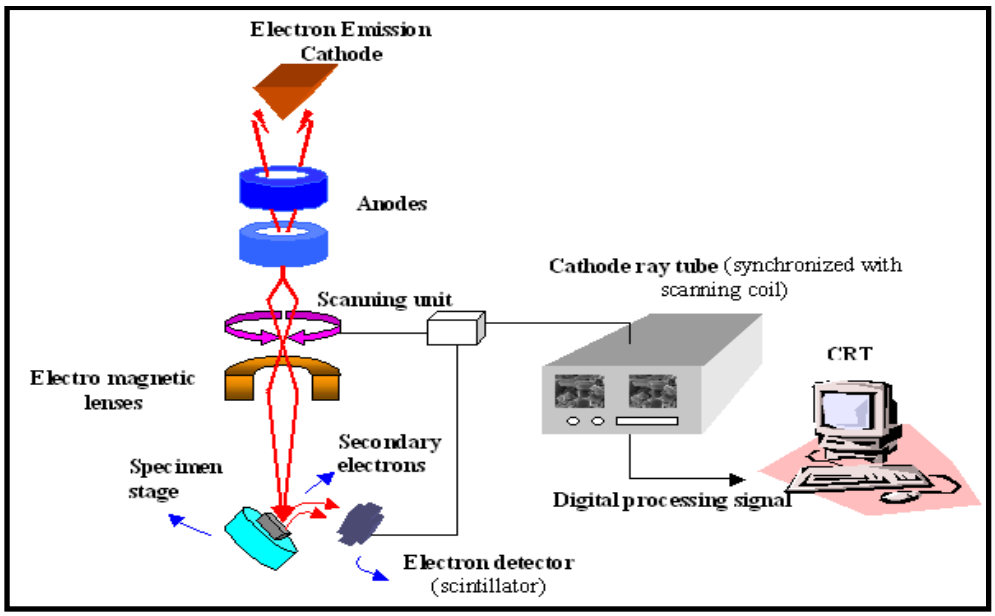

Fig.6 *Schematic diagram of a FESEM*

Since the emitter type is the basic difference between SEM and FESEM, it is better to know more about the source. FESEM uses field emission source (FES), also called a cold cathode field emitter, since it does not heat the filament. The emission is produced by placing the filament in a huge electrical potential gradient. It is usually a tungsten wire made into a sharp point. Making the tip radius so small (~100 nm) is important since now an electric field can be concentrated to an extreme level, eventually becoming so large that the work function of the material is lowered and electrons are ejected from the cathode. The concept of field emission avoids the problems faced by thermionic emission and also produces cleaner images with lesser electrostatic distortion.

A.2.2.2 <u>EDX, Elemental Mapping:</u> Energy Dispersive X-ray Spectroscopy (EDX or EDAX or EDS) is a useful tool for elemental analysis or chemical characterization of a sample. It analyzes the X-rays emitted by the sample in response to being hit by charged particles. The basic principle behind this technique is quite simple. Since every element has a unique atomic structure, the X-rays emitted by an element are characteristic of

itself, which enables one to distinguish between elements. Usually, an EDX is attached to a SEM or FESEM, although free standing EDX are also available.

It is also possible to map the elements in a SEM. One of the types of electrons emitted by the sample due to the electron beam is secondary electron, the emission of which creates internal electronic transition that gives out photons of different energies. If the microscope is equipped with an X-ray spectrometer, then one can detect the characteristic X-rays emitted from the sample surface and the elements present can be quantitatively detected. This kind of analysis is known as elemental mapping.

A.2.2.3 Photoluminescence:

In photoluminescence (PL), a material absorbs photons and then re-emits photons. This occurs when an electron is excited to a higher energy state by radiating light on the sample and then allowed to relax back to its original state, with the emission of a photon does not change significantly during a photon absorption process.

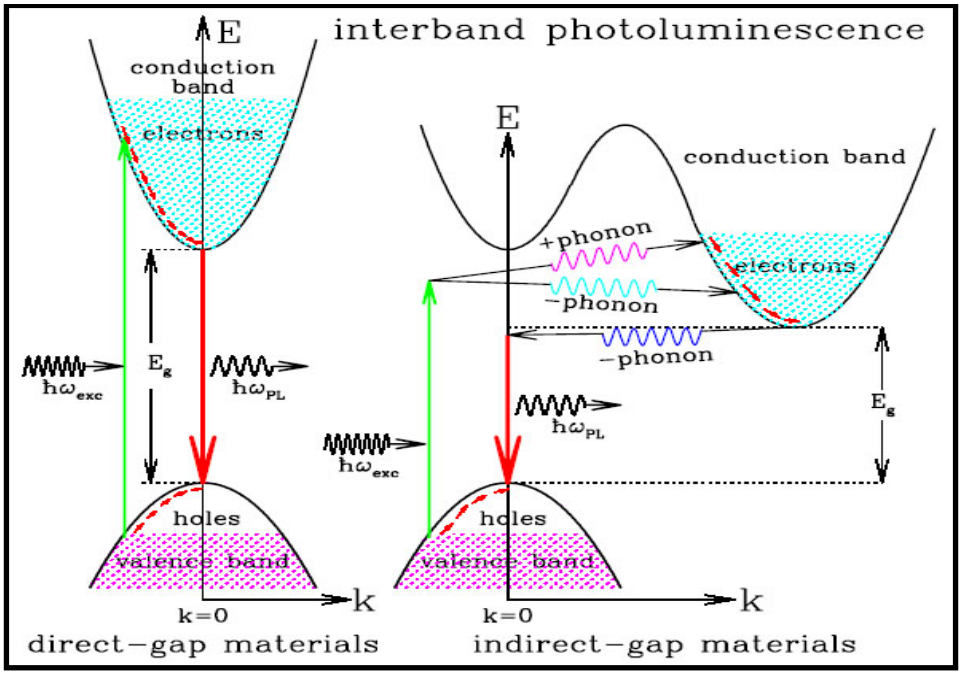

Fig 7 *Schematic band diagrams for the photoluminescence processes in a direct band gap (left) and an indirect band gap (right) material.*

If the substrate were to undergo energy transitions before re-emitting the energy, more interesting effects are observed. One of the most common effects is fluorescence, which is also very fast, but some of the original energy gets lost before re-emission and hence the photons radiated from the sample are of lower energy than the incident photons. Such photons are then said to be red-shifted with respect to the incident ones.

Time resolved Photoluminescence (TRPL) is another method, mostly used in the case of III-V semiconductors to measure the minority carrier lifetimes. The sample is excited with a light pulse and then the decay in photoluminescence with respect to time is measured.

A.2.2.4 Absorption: Absorption spectroscopy or reflectance spectroscopy is carried out in ultraviolet-visible region of the spectrum. For this reason, it is also known as ultraviolet-visible or UV-Vis spectroscopy for short. This is a complementary technique to the fluorescence spectroscopy – in fluorescence spectroscopy one studies electronic transitions from excited to ground state while in absorption it is from ground state to the excited state.

A.2.2.4.1 Reflectance measurement: The UV-Visible spectrophotometer can also be configured to measure reflectance. In such a case, the instrument will measure the intensity of light reflected from a sample (I), and will compare it to the intensity of light reflected from a reference material (I_0). This ratio, I/I_0, is called the **reflectance**, and is usually expressed as a percentage (%R).

A.2.2.5 XRD: X-ray Diffraction (XRD) is a non-destructive technique used mainly to determine the phase of a crystalline material. It can give information on unit cell dimensions too.There are primarily three types of diffraction techniques based on X-rays: a) Single crystal X-ray diffraction, 2) Powder diffraction, and 3) High- resolution X-ray diffraction.

X-ray diffraction is based on constructive interference of monochromatic X-rays and a crystalline sample. A cathode ray tube (CRT) is used to generate X-rays, which are then filtered to produce monochromatic radiation, collimated to concentrate and then directed towards the sample. If the wavelength of the incident radiation matches the diffraction angle and the lattice spacing via Bragg's law ($n\lambda = 2d\sin\theta$), then constructive interference takes place and a diffracted ray is emitted. Many diffracted rays are collected by scanning the sample through a range of 2θ angles and counted. For a powdered sample, this method works pretty well since the orientation of the sample is random and all the possible diffraction directions of the lattice should be attained. Identification of the material is done by assigning d-spacing values to the diffraction peaks, as every material has a unique set of d-spacings.

A.2.2.5.1 High-Resolution XRD (HR-XRD): HRXRD is mostly used to determine the properties of thin epitaxial films. The many methods which make HRXRD useful for studying epitaxial films are – rocking curves, ω-2θ coupled scans, reciprocal space maps and reflectivity scans. The major advantage of HR-XRD over a conventional XRD is the amount of resolution it provides in the pattern, which may go up to as sharp as 10 arc-sec.

Rocking curves are done by fixing the incident angle (ω), and varying the reflected angle (2θ). If the peak does not occur when the reflected angle matches the incident angle, then the sample is not mounted properly. A rocking curve also indicates the validity of the assumption that the sample surface is perfectly flat.

A.2.2.6 RHEED: Reflection High Energy Electron Diffraction (RHEED) is a versatile analytical tool for *in-situ* characterization of thin films during their growth by molecular beam epitaxy. RHEED is particularly suited to this application because it does not block the direction vertical to the surface of the crystal which is observed, and is very sensitive to surface roughness, down to monolayer sensitivity. The periodic variations of the RHEED intensity (so called RHEED oscillations) allows one to monitor the growth rate of layers of atoms on the surface.

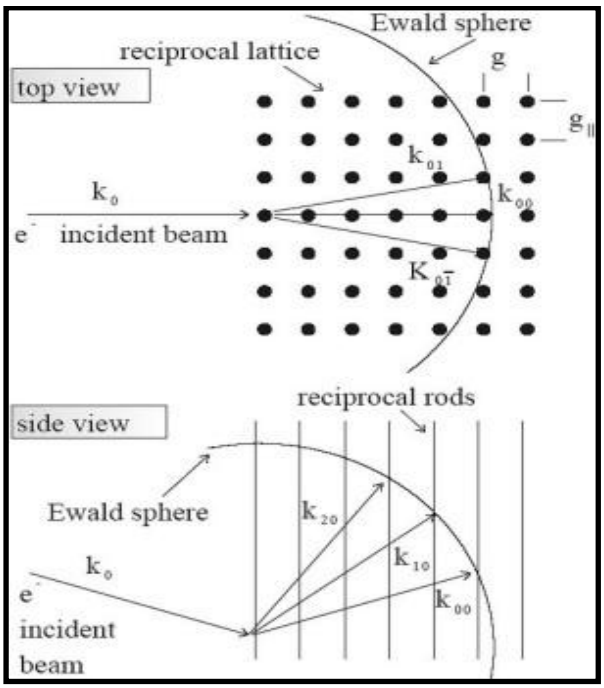

Fig.4 *The figure shows the surface of the sample in reciprocal space. The two-dimensional array of the surface atoms turn into vertical lines in reciprocal space, the reciprocal rods.*

The scattered electron beams hit a fluorescent RHEED screen in certain RHEED spots, lying on so-called Laue circles which are numbered starting from 0. In **Fig.8**, the red lines indicate Laue circles no.0 and blue lines no.1. These spots form the characteristic RHEED pattern depending on the morphology and roughness of the sample surface. Smooth surfaces can even give streaks, if the Ewald sphere cuts the reciprocal rods not at one point, but as a tangent. This makes RHEED such a powerful tool for *in-situ* analysis of thin film deposition. One single oscillation of the intensity usually corresponds to the completion of a single monolayer (**Fig.10**).

A.2.2.7 XPS: X-ray Photoelectron Spectroscopy (XPS), also known as ESCA (Electron Spectroscopy for Chemical Analysis) is one of the most widely used surface analysis techniques due to its relative simplicity in use and data interpretation. Developed in mid 1960s by K. Siegbahn and his research group, the basic working principle of XPS is the photoelectric effect outlined by Einstein in 1905. For XPS, the common photon energies are the ones emitted by Al K_α (1486.6 eV) and Mg K_α (1253.6 eV). Ti K_α (2040 eV) is another X-ray line which is sometimes chosen. The reason why XPS is highly surface sensitive is because the photoelectrons which are excited from the solid are of very short range. The binding energy of these peaks are the characteristic of the element. The composition of the material's surface can then be obtained by calculating the area of the peaks with appropriate sensitivity factors. The shape and the binding energy associated with each peak can be slightly altered by the chemical state of the emitting atom, which use of XPS, finding the chemical bonding information.

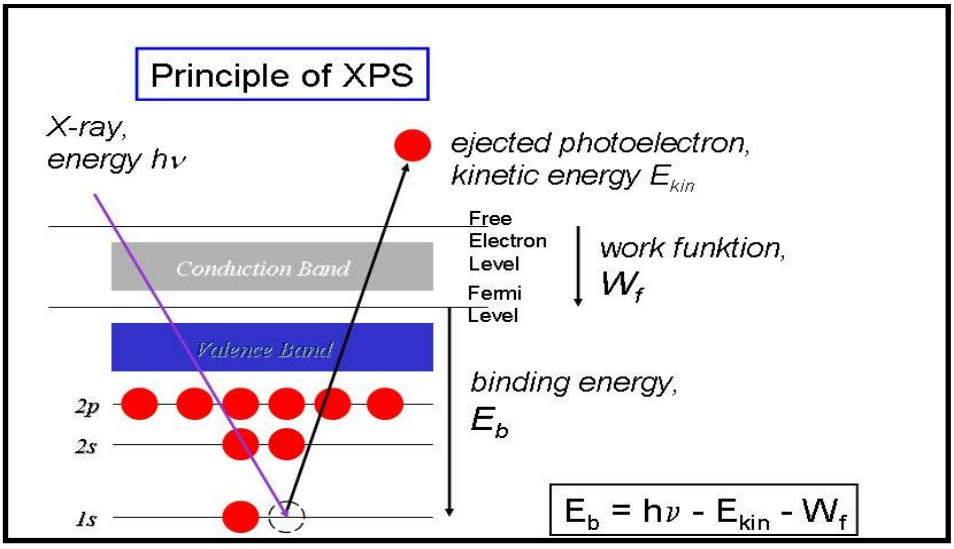

Fig.8 *Principle of XPS – photoelectric effect is shown*

Apart from detecting X-rays, the Auger electrons can also be detected, which is an additional advantage of XPS. As mentioned before, an atom's oxidation state, chemical bonds and crystal structure can give a shift in the binding energy. This shift is known as *chemical shift*, and it is easily detected in XP-spectra, because the technique is of high intrinsic resolution (since core levels are at discrete, well-defined energy levels) and is a one-electron process (which gives an ease in interpreting data).

Fig.9 *XPS instrument used in the present study – purchased from Brüker, Germany.*

A.2.2.8 AFM: The Atomic Force Microscope was developed to overcome a basic drawback with STM – that it can only image conducting or semiconducting surfaces. The AFM, however, can image almost any type of surface, including ceramics, glass, polymers, composites and biological samples by measuring the electrostatic force between the tip and the sample atoms. A laser is reflected from the back of the reflective AFM lever onto a position-sensitive detector. The tips and cantilevers are these days fabricated from either Si or Si_3N_4. The tip radius typically varies from a few to 10s of nm.

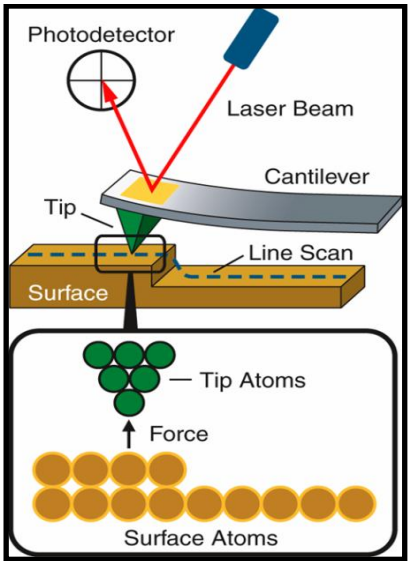

Fig.10 *Principle of an AFM – laser beam is reflected from the back of the cantilever and is detected by a photodetector. The tip is extremely sharp with a single atom at the tip end*

As mentioned above, the force between the tip and the sample is calculated by measuring the deflection of the lever, and finding the stiffness of the cantilever. From Hooke's law, we have F= -kz, where F is the force, k is the stiffness of the cantilever and z is the distance the lever bends.

Chapter A.3

Results

A.3.1 Growth of GaN on c-plane sapphire by MBE

The MBE growth chamber base pressure was maintained at ~5.1×10^{-11} Torr by using turbo-molecular pump backed by molecular drag pump, along with cryogenic pump, ion pump and titanium sublimation pump. The c-plane sapphire (Al_2O_3) surface was pre-cleaned in preparation chamber where it was degassed at 500^{o}C for 30min, followed by degassing in growth chamber at 800^{o}C for 10min. The RF plasma generator was used to create nitrogen (N_2) plasma at forward power (W_f ~ 375 watts), reflected power (W_r ~6 watts), nitrogen flow rate was kept constant at ~4.4 sccm and nitrogen pressure ~2.5×10^{-5} Torr during the growth of GaN. This high nitrogen pressure was used to promote 3D nanostructure formation by not allowing Ga adatoms to diffuse long before they are nitrided. To maintain a clean environment continuous flow of liquid nitrogen was maintained in the cryopanel.

After cleaning the sapphire substrate, its temperature was kept constant at 630^{o}C. Ga k-cell (1000^{0}C) shutter was opened simultaneously along with the nitrogen plasma source. The GaN growth was done at a growth rate of 0.4 µm/hr. The growth time was 8 hours, which resulted in a ~3.2 µm thick film. The morphology of the film was observed by FESEM, the crystalline quality determined during growth by RHEED and CL spectroscopy was performed after growth to determine the optical quality of the film.

A.3.2 Properties of the GaN film

1. <u>FESEM:</u> All the FESEM images were taken with a *NOVA NanoSEM 600* machine purchased from FEI, Netherlands. The images of fresh GaN film show the presence of a network-like structure. A tilted view shows that the network is actually made up of walls which taper as they go up. The thickness of the walls was measured to be of the order of a few nanometres at the top. The photoluminescence spectra showed a high intensity band edge emission at ~363nm, fairly well in keeping with the literature values. The reflectance spectra showed a dip at 354nm, and one more at 679nm. XPS measurements showed the presence of both gallium as well as nitrogen. The thickness of the film was 3μm, hence the peaks corresponding to Al and O from the sapphire substrate were not observed. XRD pattern taken of the film re-confirmed the fact that the gallium nitride film was single crystalline wurtzite in nature and grew in the same c-plane direction as the sapphire.

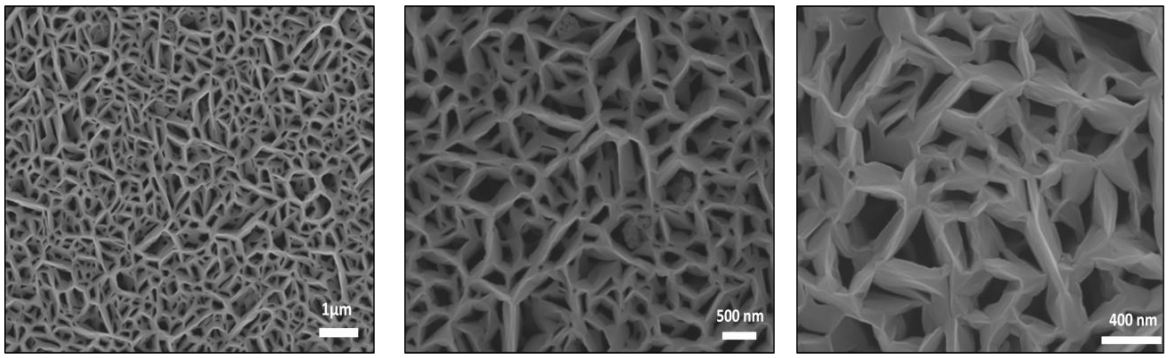

Fig.1 *FESEM images of fresh grown GaN on c-plane Al_2O_3– network shape can be seen*

2. <u>HR- XRD:</u> The HR-XRD patterns were taken using a *D8 advance* instrument obtained from Brüker, Germany. The pattern of the fresh GaN film is shown in Fig.2. There are five peaks, three of which are of GaN at 34.5°, 72.7° and at 126.1°. These three peaks are indexed as the (0002), (0004) and (0006) faces of the wurtzitic GaN crystal, respectively. The two

other peaks belong to sapphire, at 41.7° and 90.7°. These peaks are indexed as (0006) and (000 12) faces of the c-plane sapphire substrate. The peaks and their intensities show that the GaN film is wurtzite with its c-axis perpendicular to the c-plane of the substrate. The FWHM of the Ga (0002) peak in the ω-mode scan was around 2800 arc sec, while for all the sapphire peaks the value was 72.

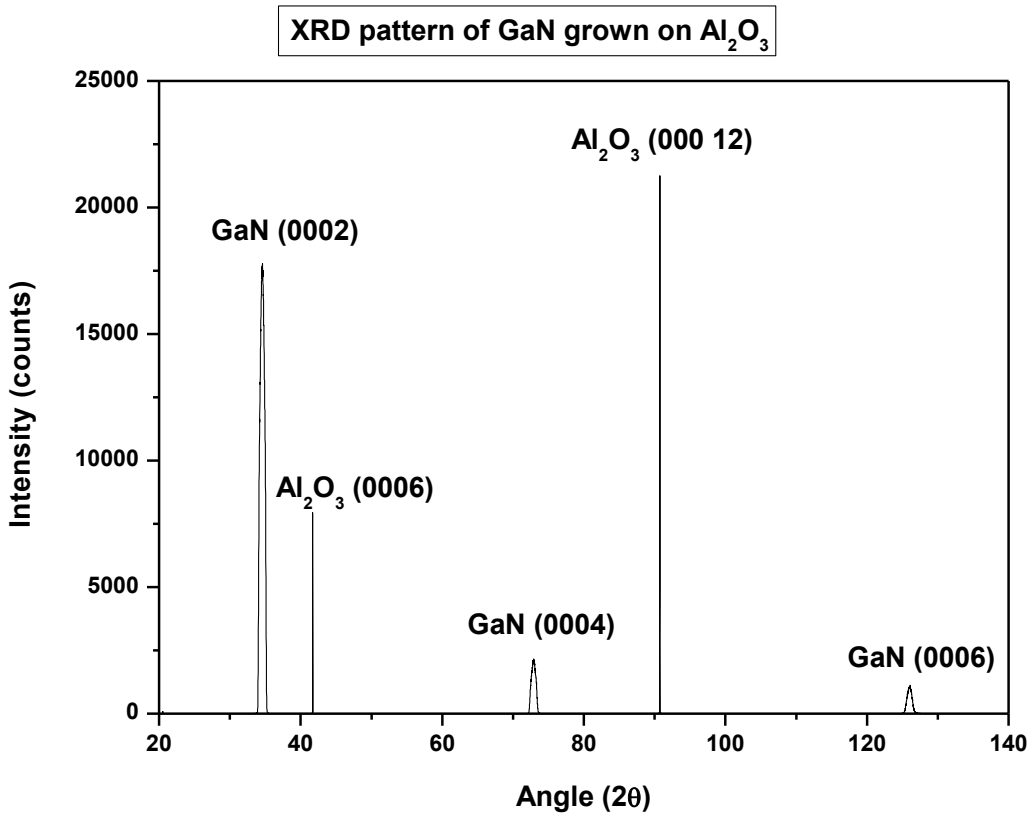

Fig.2 *XRD pattern of the GaN substrate*

3. <u>Absorption:</u> Absorption spectrum of GaN film was taken using a Perkin Elmer *Lambda 900* UV/Vis/NIR spectrometer kept in the reflectance mode. The spectrum showed a dip at 354nm, indicating that the sample absorbs at this value. Hence, for the photoluminescence studies done later, a wavelength lesser than 354 nm was chosen for excitation to get the best cross section for the PL spectrum.

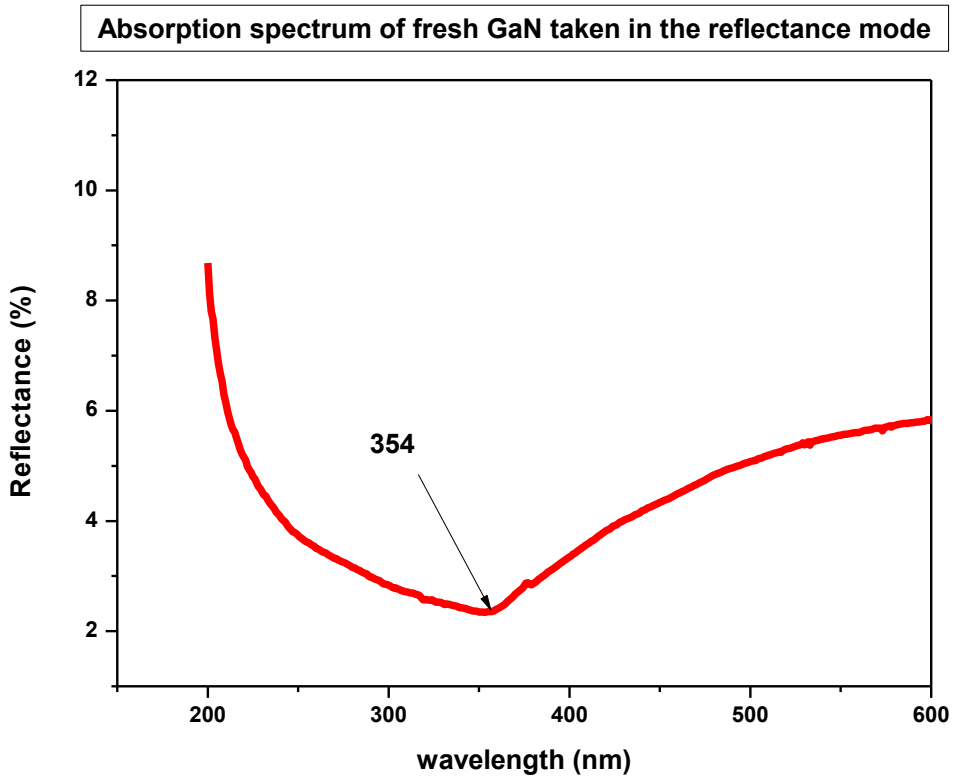

Fig.3 *Absorption spectra of the GaN sample taken in the reflectance mode. A dip is observed at 354 nm.*

4. <u>Photoluminescence:</u> The photoluminescence spectra were taken on a Perkin Elmer *LS 55* Luminescence Spectrometer with an excitation wavelength of 325 nm and slit sizes of 10 mm each. For the GaN film, a strong peak at 362.7 nm was observed, attributed to the band edge emission (band gap = 3.4eV). The actual band edge of bulk GaN is at 364 nm, and this small shift can be due to the tapering nanowall structure (as seen in FESEM images of Fig.1) which can show some blue shift at its apex. More peaks were observed at higher wavelength values, around 443, 483 and 531nm which were due to the defects in the GaN film. The ratio of the band edge emission peak to the three defect peaks was 11:1, 14:1 and 29:1 respectively. Hence, it can be concluded that the GaN film was grown with very little defects.

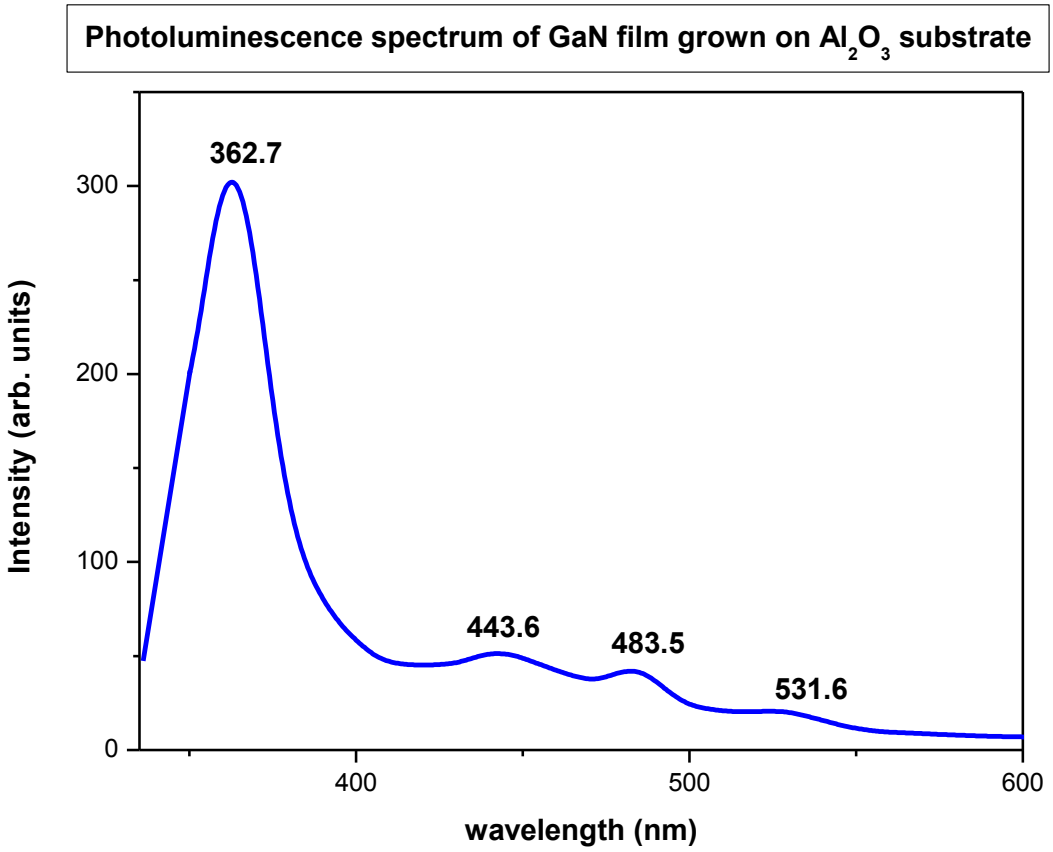

Fig.4 *Photoluminescence spectra of GaN*

5. <u>RHEED:</u> The RHEED pattern shows dots, which are typical of transmission pattern. This means that the sample surface is not flat, but rather rough in nature. A more interesting feature is that the spots are not circular, but seem to be flattened in one direction (anisotropic). This is attributed to the misalignment of the nanowalls. The ratio of the distance between the spots horizontally and vertically is 1.64, which corresponds to the wurtzite crystal structure.

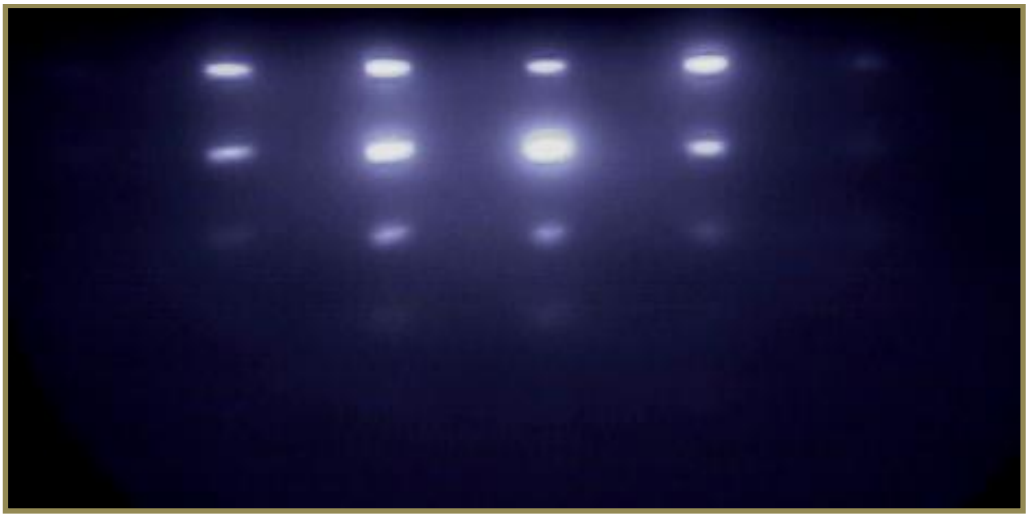

Fig.5 *RHEED pattern of the GaN film grown on c-plane sapphire*

6. XPS: The general scan of the GaN sample is shown in Fig.6. Peaks of the major elements detected in the sample are marked. The most intense peak of Ga is that of the $2p_3$ orbital, and occurs at 1118eV. In this case the peak is seen at 1124eV, because of the carbon shift. In the spectrum, carbon correction is done to get the peaks at the right value. The most intense peaks for N, C and O are 1s orbital peaks, occurring at 396eV, 285eV and 530eV. The intensities of these peaks are used to calculate the % composition of the elements. Due to handling the sample in air, carbon contamination was detected on the film, since XPS is a highly surface sensitive technique. It was possible to get rid of the contamination via sputtering (spectrum not shown here).

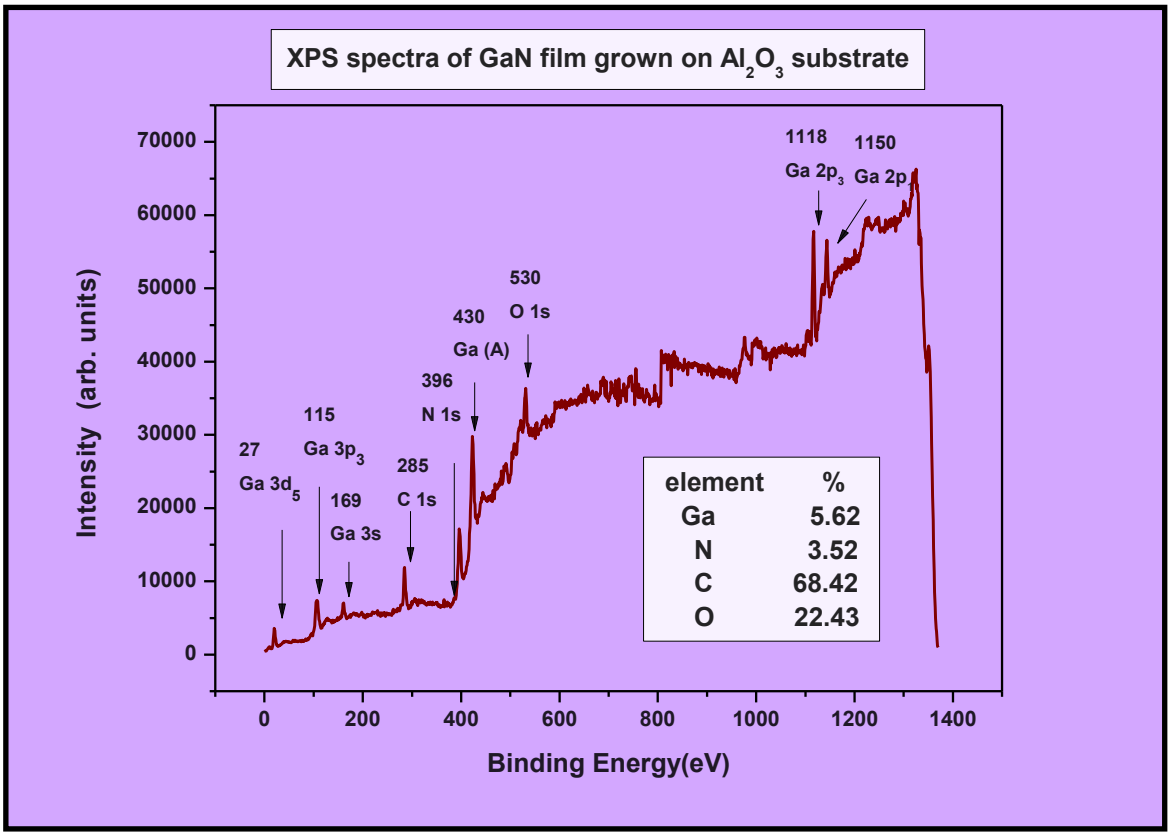

Fig.6 *XPS spectrum of GaN*

A.3.3 Deposition of Ag nanoparticles on GaN network:

The experiment consisted of 3 parts:

1. Deposition of silver particles on GaN
2. Characterization of the sample
3. Annealing the samples to different temperatures and characterizing at each step

1. The deposition of silver nanoparticles was carried out in two ways – (i) a chemical route, using electroless deposition technique, and (ii) a physical route, using physical vapour deposition. Steps 2 and 3 were repeated in both the cases.

A.3.3.1 Chemical route:

Procedure:

a.Sample preparation: -

(1) **Cleaning**: The gallium nitride sample was thoroughly cleaned by dipping in ethanol, isopropanol and acetone, in that order (all chemicals from Sigma Aldrich), and sonicating for 4 minutes each time. The samples were rinsed with deionized water after each sonication. This ensured that no dust was present on the surface when carrying out the experiment.

(2) **Sensitizing:** Next, the samples were kept in a solution consisting of 22mM $SnCl_2$ (dehydrate 99.995+ % pure, Aldrich) and 70mM CF_3COOH (98% min, titration grade, Aldrich) in a 50:50 (v/v) deionized (DI) water/methanol solution for 60 min.

(3) **Activation:** The samples were then kept in an activation solution of $AgNO_3$ (98+%, ACS grade, Aldrich) in NH_4OH (certified ACS, Fisher Scientific) for 10 min. The activation required the formation of a $[Ag(NH_3)_2]^+$ complex, which was prepared by the dropwise addition of NH_4OH, causing the solution to change colour from clear to cloudy and brown, and then back to clear.

(4) **Plating:** This is the most important step in the process, which determines the actual deposition of Ag particles on the GaN surface. The activation solution was taken, with the GaN samples already dipped in it, and formaldehyde (conc. range from 8mM to 20mM) was added dropwise. A dropwise addition of formaldehyde provides control over the amount which goes into the solution, and hence a handle on the concentration of silver particles reduced. The plating was done at a temperature of 4°C, and the pH was maintained between 9.5 and 10. Although plating was possible with a wider range of pH (9-11*) but we observed that the range that we took was optimal to avoid the formation of islands which were too big and agglomerations. The time of plating was also varied from 15 min to 12 h. Reaction time and concentration of formaldehyde depended on the amount of Ag deposition required. After the Ag particles' deposition, the substance was rinsed with deionized water.

b.Characterization:-

Surface morphology was characterized by using Scanning Electron Microscopy (SEM) and Field Emission Scanning Electron Microscopy (FESEM). All images were taken using 10-15kV accelerating voltage, working distances ranging from 5-25mm, and magnifications ranging from 5 000x to 300 000x. A thin strip of carbon tape was stuck to the sample when loading onto the stub, in order to prevent electron beam drift and charging. Energy Dispersive X-ray Spectroscopy (EDAX or EDX or EDS) was carried out to confirm the purity of the sample after deposition of Ag particles on the substrate. X-ray Photoelectron Spectroscopy (XPS) was also used to confirm the deposition of Ag on the surface without any impurity. In this technique, Al K_{α} (1486.5eV) was used as a source for the generation of X-rays, and the kinetic energy of electrons was detected by a hemispherical band pass analyzer. Photoluminescence studies have been done on each sample, excitation wavelength 325nm,

excitation slit width 10nm, emission slit width 10nm, 350nm cut-off has been used and the scan speed was 200nm/min.

c. Results : -

1. SEM: SEM images of the silver deposited GaN were taken using an *S440i* instrument purchased from *Leica Technologies*, UK. Fig.7 (a) shows the general image of the reported surface. The silver was observed to have been deposited quite uniformly, although the entire GaN surface was not covered. Fig.7 (b) shows some particular areas of the sample, where large clusters of silver with sizes ranging in a few microns were seen. The individual particle size ranged between 100-600nm.

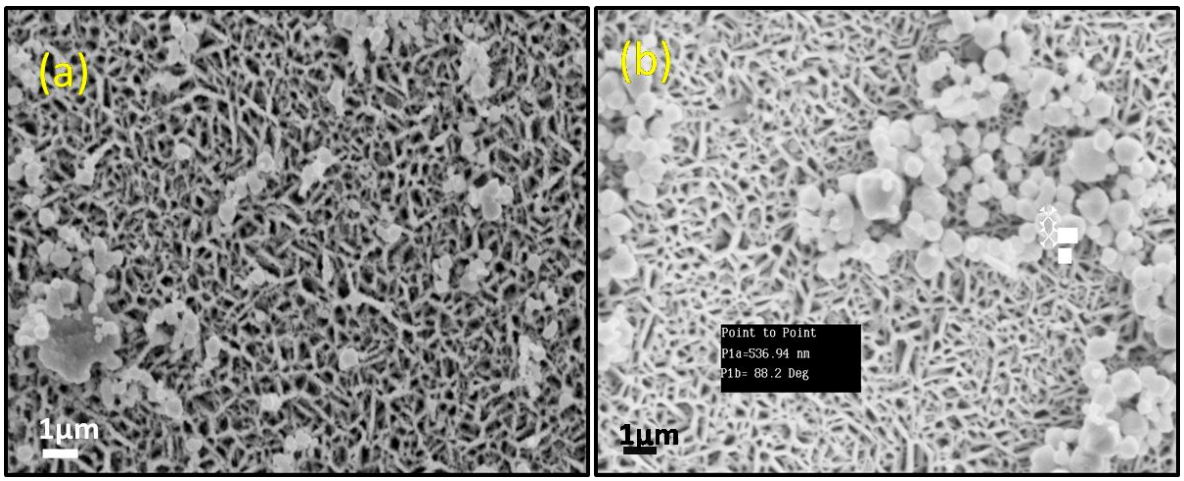

Fig.7 *SEM images of as- deposited Ag on GaN network. The silver spread all over the surface, and in some places cluster formation was observed.*

2. EDX: The EDX pattern was also taken by zooming in on the agglomerated particles on the substrate. An instrument purchased from Brüker was used for this purpose. The resolution of the instrument was 0.129eV. Fig.8 shows the EDX pattern with quantification shown in the inset. EDX confirmed the purity of the sample better than the XPS, since it gives information from relatively

deeper into the sample. Gallium being the most sensitive shows the highest peak, while N and O show very small peaks. The size of the peaks is not an indication of the concentration of the element, since every element has different sensitivity. The quantification shows a ratio of Ga:N = 48:44, with silver present and oxygen as the only impurity.

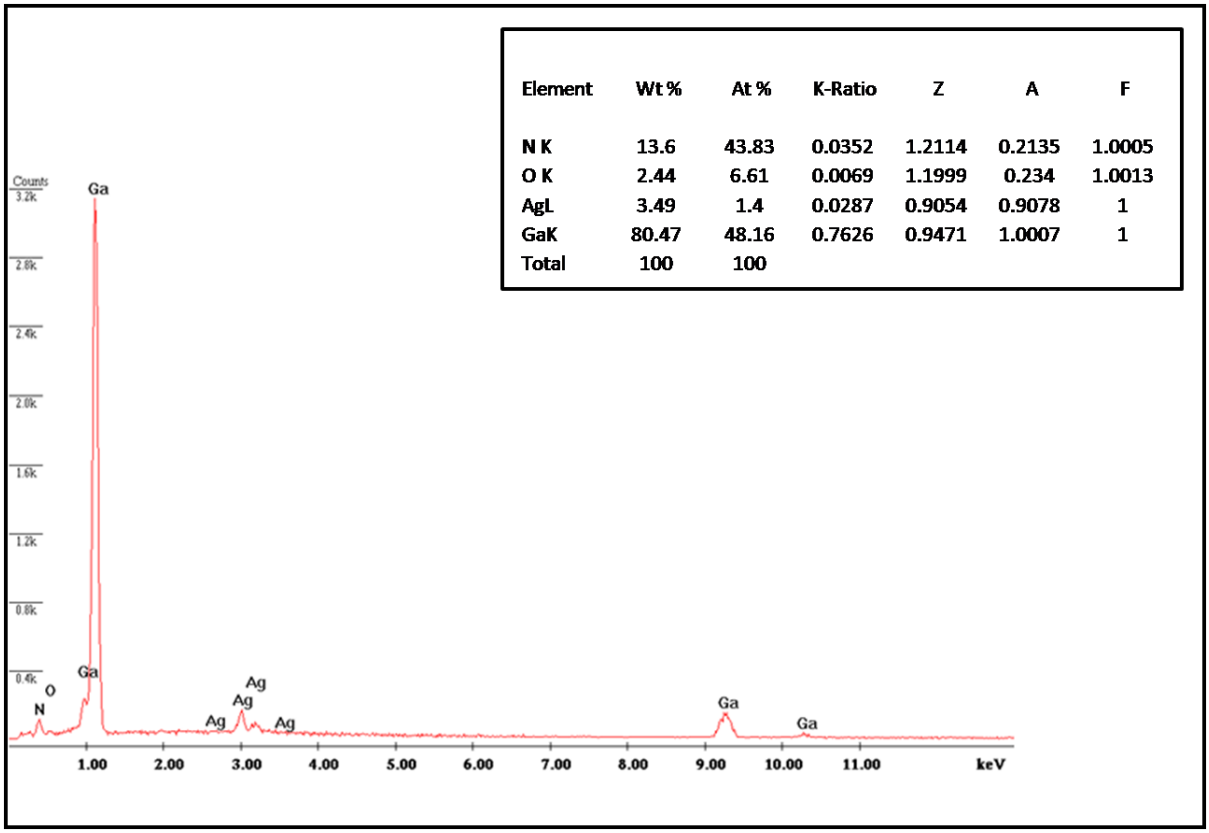

Fig.8 *EDX pattern of the Ag deposited GaN network. It shows that silver has been deposited on the network without many impurities.*

3. XPS: Fig.9 shows the XPS spectrum of the sample after Ag was deposited on it. The characteristic doublet of Ag $3d_3$ and $3d_5$ peaks at 368 nm and 374 nm can be clearly seen. The intensity of this doublet meant that the surface was well covered with silver and that the amount of silver deposited was also very high. Other peaks were also marked, same as done for pure GaN. The impurities like carbon and oxygen were again high since sputtering was

not done, as it could have removed the silver also. The percentage of gallium is also quite low as seen in the quantification. This indicates that the thickness of silver is quite high, since very less information is obtained from under it.

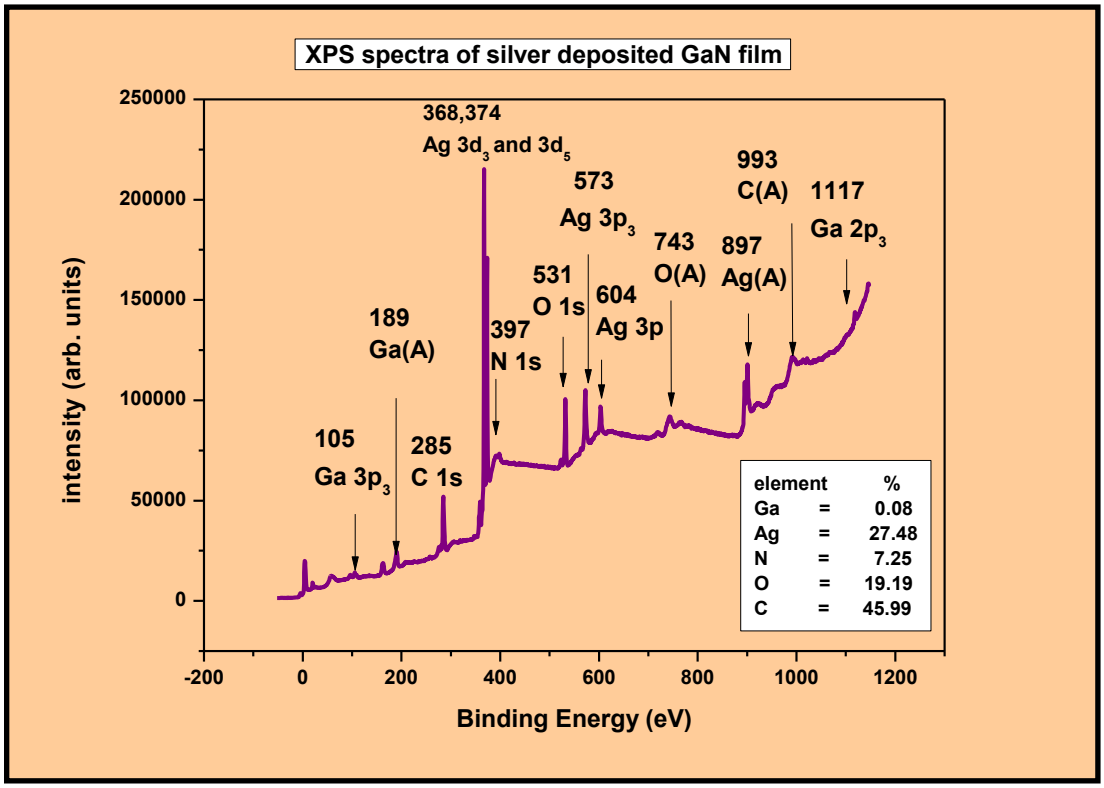

Fig.9 *XPS of the as-deposited Ag particles on GaN network. The silver peak is of appreciable intensity, confirming that silver is present on the GaN*

Annealing: The samples were then annealed at temperatures of 200°C, 400°C, 600°C and 700°C. Characterization was done for all the samples by employing different techniques described earlier.

(a) **SEM:** It was observed that with annealing, the islands break apart and form smaller clusters. Fig.10 shows the effect of annealing on the silver particles present on the surface. At 200°C (Fig10 (a)), the clusters are still present, though they seem to be breaking up. As we go on annealing to even higher temperatures, the clusters result in individual particles, as we can see in Fig.10 (b), which shows the SEM image of the sample annealed at 400°C. At a

temperature of 600°C, the clusters completely break up into particles of sizes ranging from 100-500 nm, as seen in Fig.10 (c). Upon reaching a temperature of 700°C, the silver completely wets the surface, as though becoming absolutely liquid, though some larger particles are still seen (Fig.10 (d)). This shows that the annealing of the sample after depositing silver follows a pattern, where large clusters break up and eventual wetting of the surface takes place.

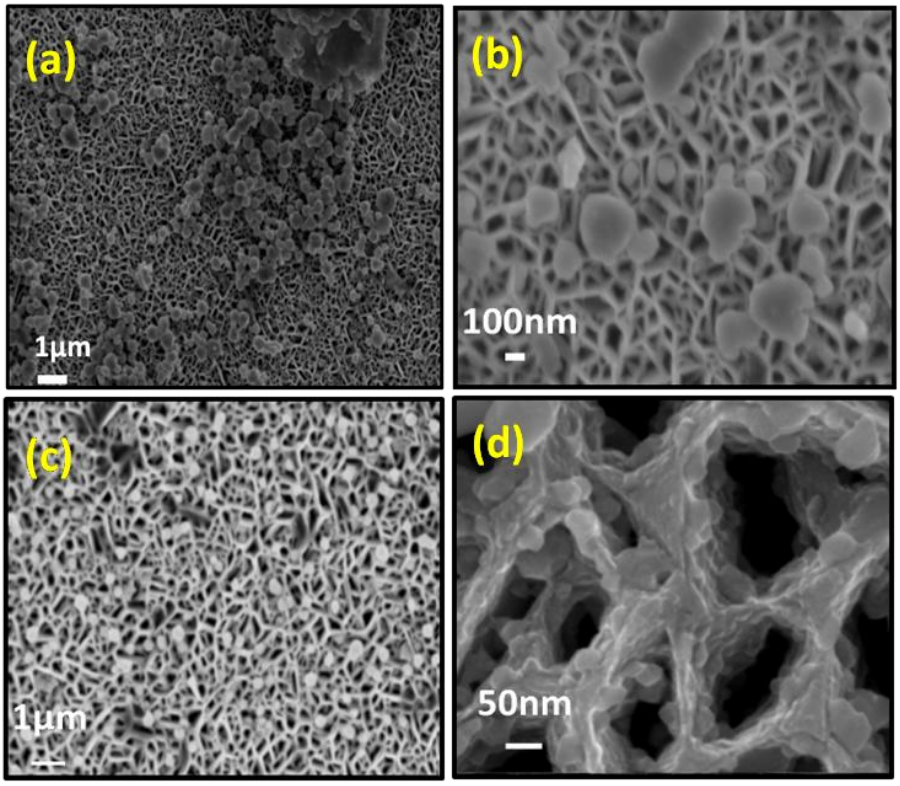

Fig.10 *SEM images of sample annealed to (a) 200°C, (b) 400°C, (c) 600°C, and (d) 800°C – initially clusters form, which break up into smaller particles, eventually forming a film on the surface, i.e. wetting.*

(b) **Photoluminescence:** In the photoluminescence spectra, taken on the same instrument with the same values as before, with an excitation wavelength of 325 nm, many new features were observed (Fig.11). The fresh GaN peak coming at 362 nm is shown as a reference in the figure below. The as-deposited spectrum showed quenching relative to the fresh GaN peak, but as the samples were annealed, an increase in intensity was observed. At

a temperature of 400°C, the intensity of the spectra rose above that of fresh GaN. Also, new peaks were observed to come up at 367 nm, 382 nm and 398 nm. Consequently, the area under the peak increased three fold from the original peak area of fresh GaN. Till 600°C, the rise in intensity continued, after which the spectra again quenched at 700°C.

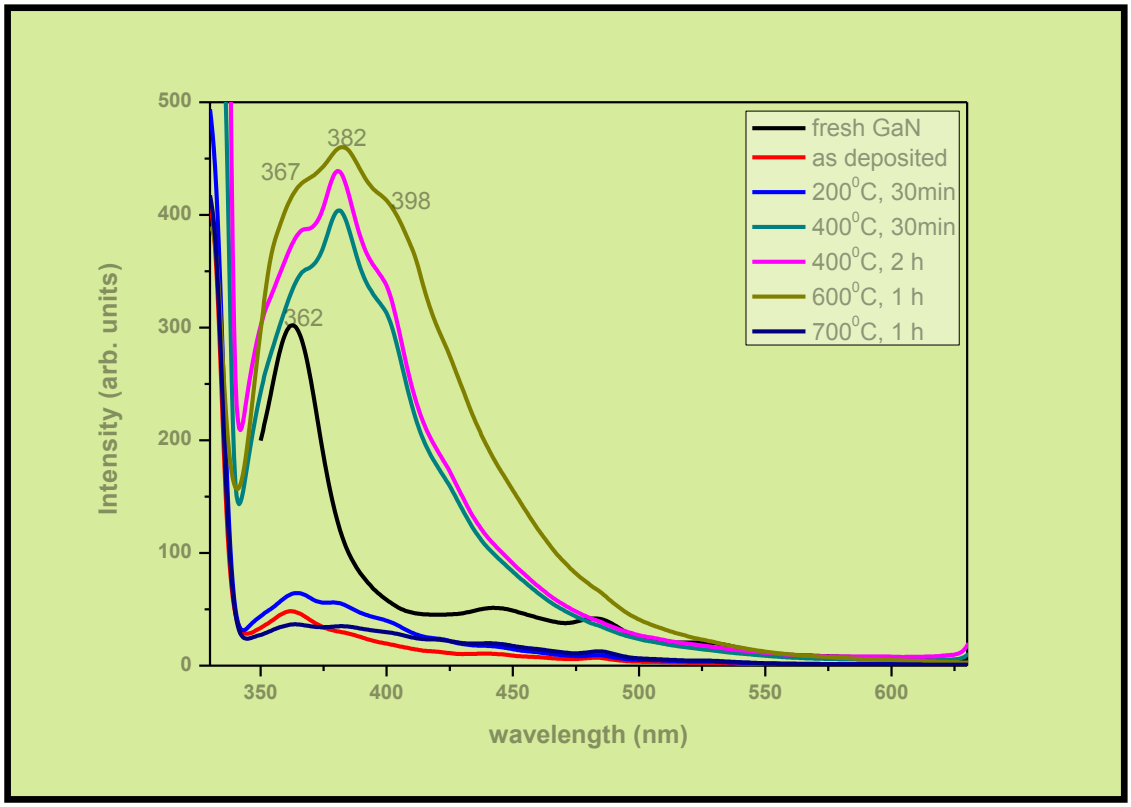

Fig.11 *Photoluminescence spectra of the sample – annealing effects shown*

(c) **XPS:** The XPS reveals that as the samples are annealed, the silver peak rises in intensity. Calculating the height of the peaks, marked as 'h' in the graph, it was observed that the intensity of the peak more than doubled (~101% to original) upon annealing twice. No shifting of the peaks was observed, indicating that no new bonds are formed (e.g. oxides).

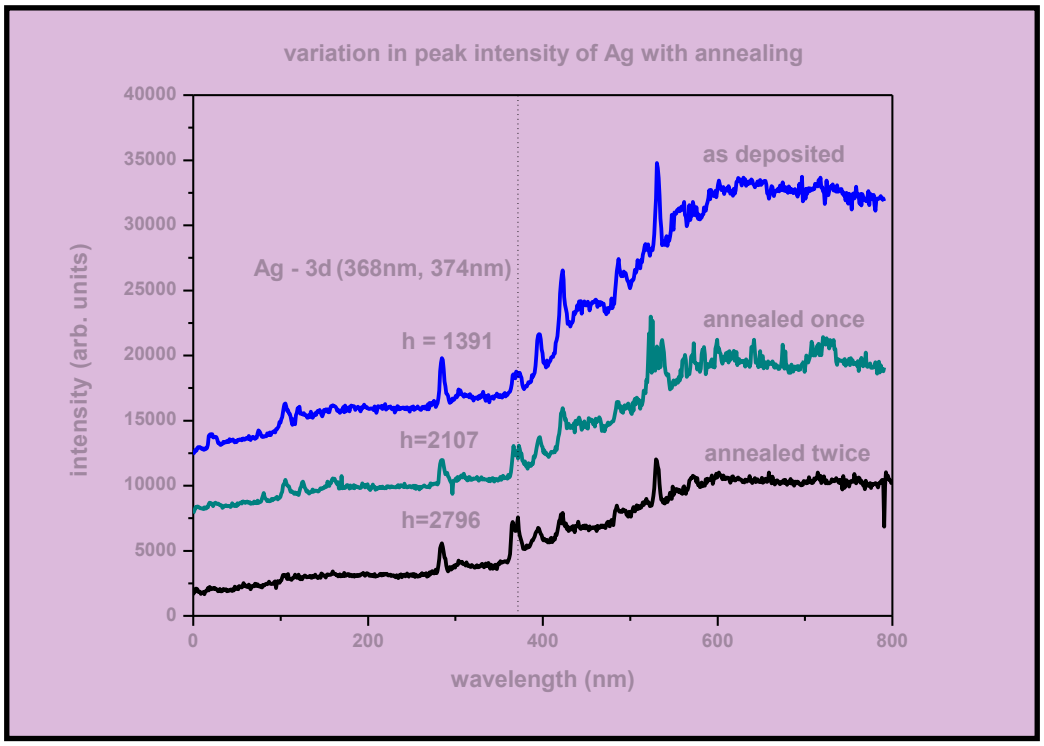

Fig.12 *XPS spectra of Ag coated GaN –annealing dependence is shown*

Another interesting observation made during the valence band scanning of the samples was that the Fermi level showed a non-zero density of states, indicating metallic behaviour. Fig.13 shows the valence band spectra taken from XPS for different depositions. In the figure, Δl gives the separation between the curve and the baseline at E_F. Valence band spectra of fresh GaN is shown for comparison. Being a semiconductor and hence a dielectric at room temperature, the density of states at E_F for fresh GaN is zero. This is indicated by a zero value of Δl. Deposition of even a medium amount of silver, however, changes Δl to a finite non-zero value. This is also intuitively obvious since the silver covers the GaN substrate completely; and hence the surface shows metallicity. Also, higher coverage shows higher metallicity.

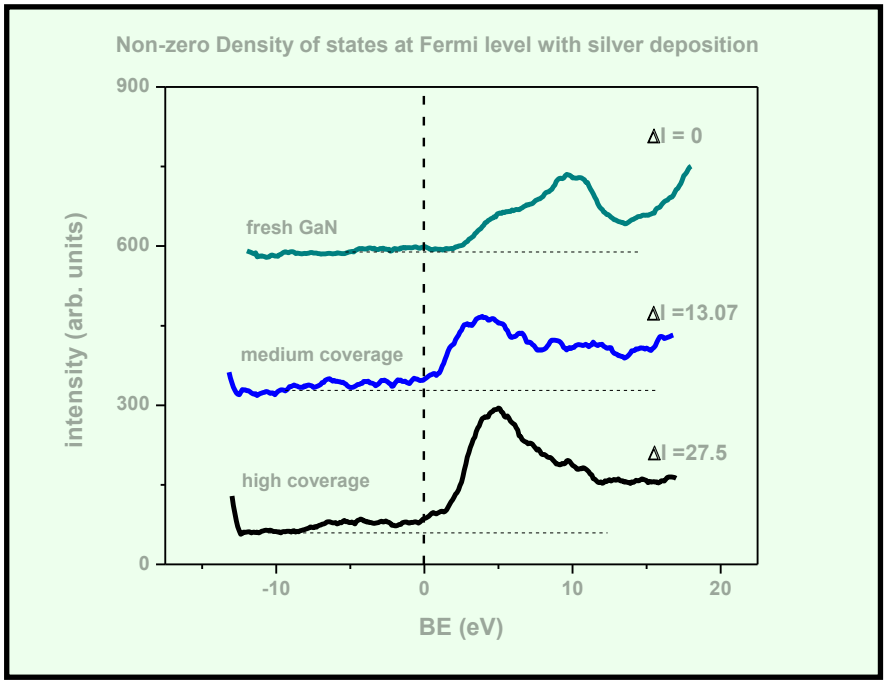

Fig.13 *Valence Band spectra of samples from XPS – coverage dependence and annealing effects shown*

(d) **PXRD:** The X- ray diffraction data did not show any difference from the GaN film, shown in Fig.14, where the (0002) and (0006) peaks of GaN are seen. This led to the conclusion that the silver particles were not crystalline, since silver is still seen in the XPS and EDX spectra.

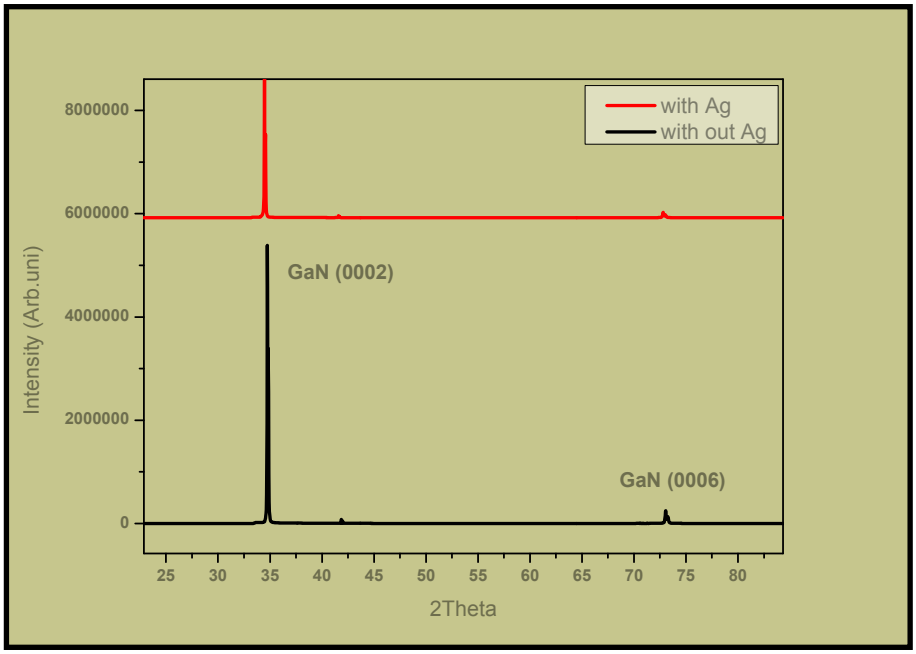

Fig.14 *PXRD pattern compared for bare GaN and silver coated GaN – no extra peaks*

A.3.3.2 Physical Route:

Electron beam physical vapour deposition (EB-PVD) was used as a physical method to deposit silver onto the GaN substrate. The source of silver was a wire (d= 0.01", 99.999% pure, Alfa Aeser).

Procedure:

An e^- beam evaporation system from SVT associates was used for this study. Silver taken was a 99.999% pure 0.1mm diameter wire. Voltage used was 5.45kV and the current was 4mA. A quartz crystal thickness monitor (QCTM) was used to measure the thickness of the deposited film. The pressure of the deposition chamber at the time of starting the electron beam was 5×10^{-7} Torr. The thickness of the silver coating was 1.3 nm, as determined by the QCTM.

Results:

The samples were characterized using FESEM, EDX and XPS. Similar to the chemical route, silver deposited on the substrate; though the uniformity was better in this case. This was observed by FESEM images. XPS and EDX confirmed the presence of silver without any contamination.

(a) **FESEM:** The images were taken using the same instrument as earlier. The silver in this case deposited much more uniformly, coating the surface completely with particle sizes being the same, around 5 nm (Fig.15). This is in contrast to what was observed for the chemical case, which showed patchy coverage (Fig.7).

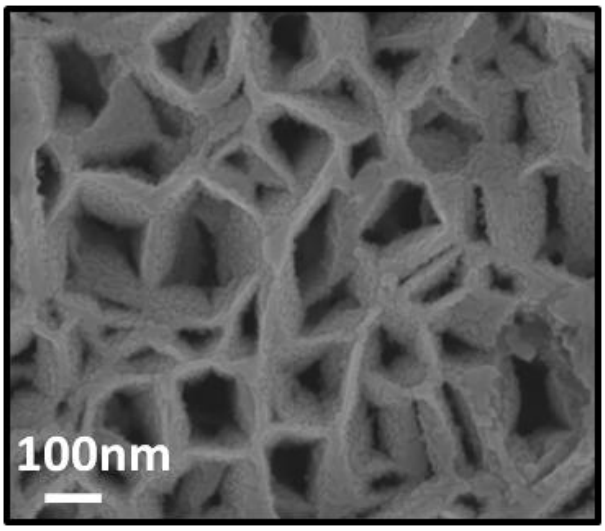

Fig.15 *FESEM image taken of the as-deposited sample – silver can be seen more uniformly spread over the walls*

(b) **XPS:** For this measurement, an XPS from Omicron Nanotechnology was used. The source used was Mg K_{α}. General scan was taken with a step size of 0.2 and a pass voltage of 5kV. Spectrum shows a highly intense silver peak, indicating the presence of silver on the substrate. Other peaks were marked as before for fresh GaN. The contaminants C and O are only on the surface, as explained earlier, and also as observed by EDX measurements.

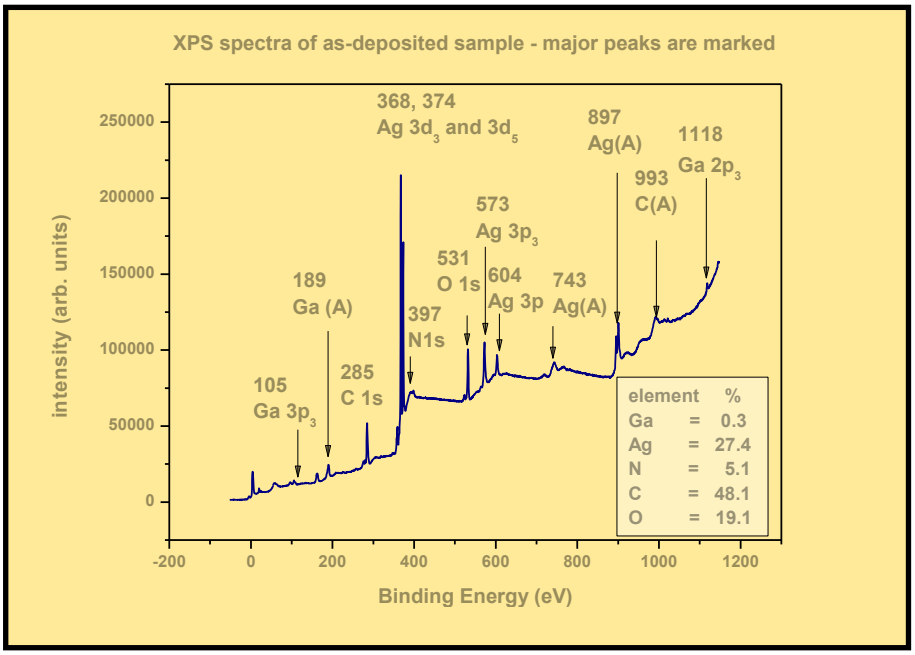

Fig.16 *XPS spectra of as-deposited sample*

(c) **EDX:** The EDX pattern, taken again by zooming in to a particle, shows the presence of silver peak, and the purity is further reaffirmed due to the absence of any anomalous peaks. The sample seems cleaner than earlier, and the Ga:N ratio is also quite balanced at about 42:44.

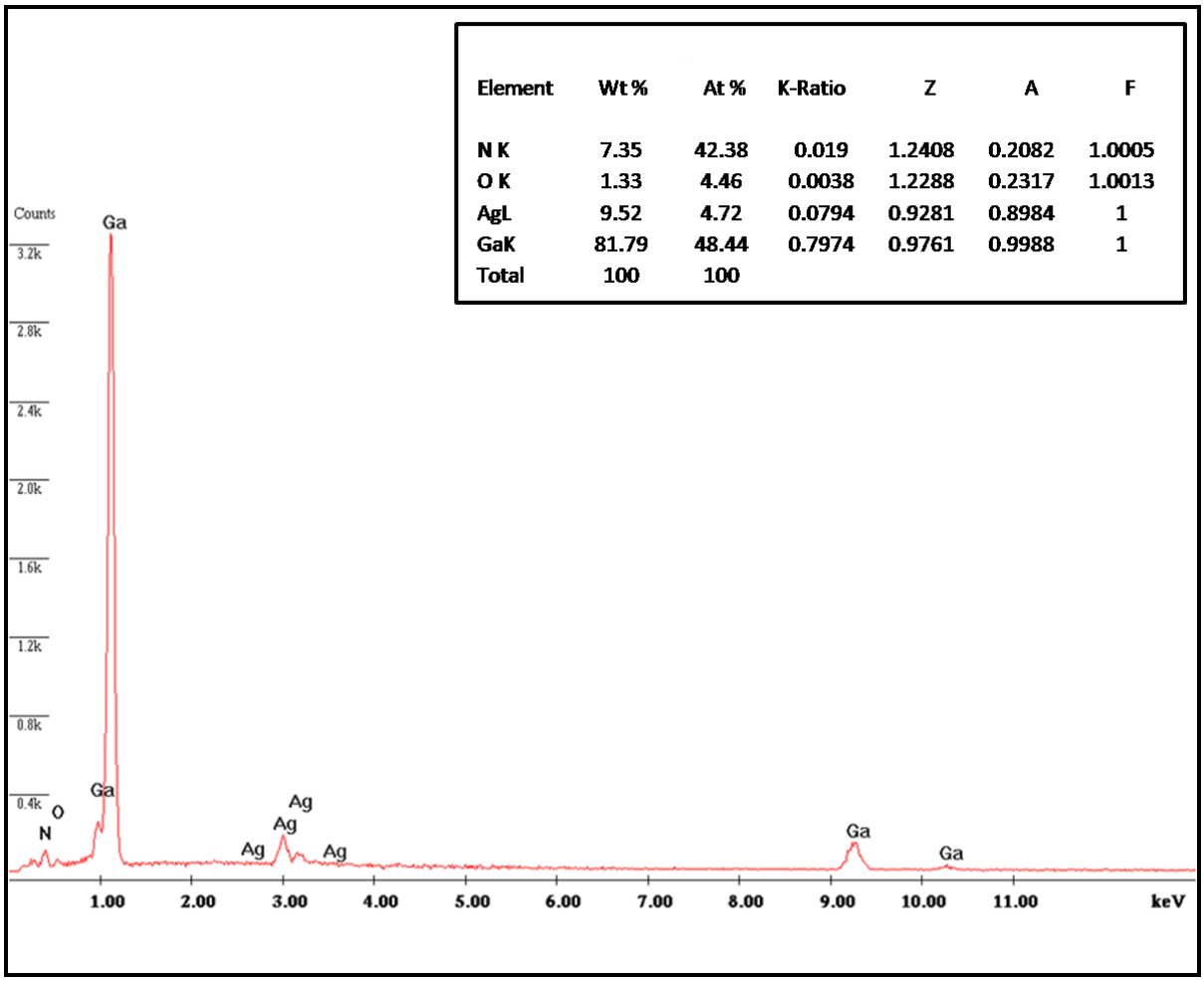

Fig.17 *EDX pattern of the as-deposited sample- inset shows the quantification*

Annealing: Samples were annealed to 200°C, 400°C, 600°C and 700°C. They were characterized using FESEM and Photoluminescence (PL).

(a) FESEM: The FESEM images taken of the samples at different annealing temperatures are shown in Fig.18. For the physically deposited system, silver initially coats the whole surface as a layer; the particle sizes being the same, at around 5 nm (Fig.15). With annealing, these silver particles diffuse along the walls and agglomerate. Fig.18 (a) shows the starting of agglomeration at 200°C, with average particle size increasing to 40 nm. However, as we increase the annealing temperature, the agglomeration is combined with a bit of wetting, as can be observed from Fig.18 (b). At 600°C, very large particles of the silver form due to the agglomeration (~50-100 nm). Eventually, when the annealing temperature is increased to 700°C, the silver completely wets the surface again, similar to the case in chemical deposition. A few large islands still remain. This was attributed to the diffusion of the particles along the walls leading to Oswald ripening. Images were also taken at a tilt of 45°C to better observe the deposition on the inside of the walls.

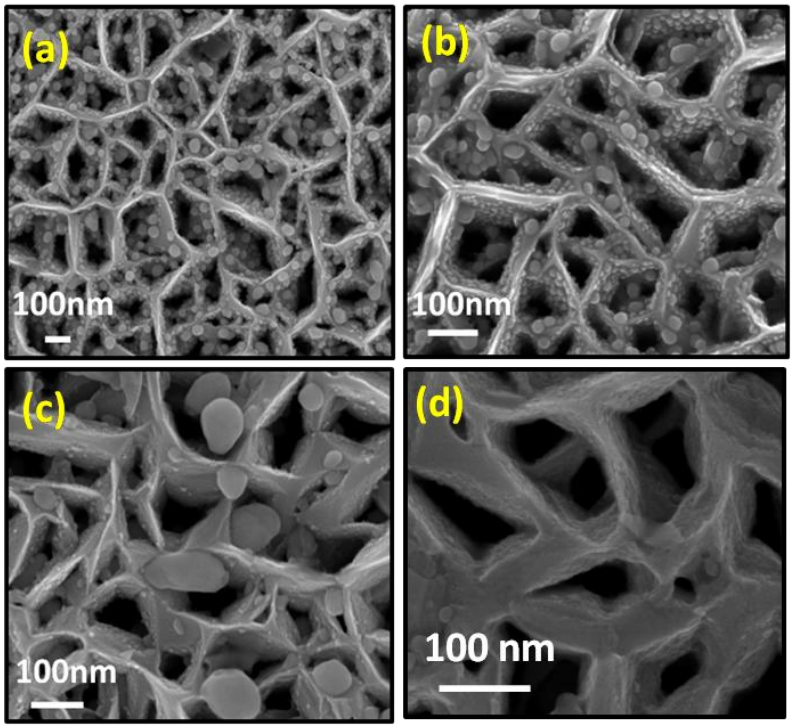

Fig.18 *FESEM images of the sample after annealing to* ***(a)*** *200°C, (b)400°C, (c)600°C and (d) 700°C – smaller particles aggregate into larger ones, but at 700°C the whole silver wets the surface.*

(b) Photoluminescence: The photoluminescence spectra of the sample showed a similar trend as it did in the previous chemical synthesis case, with initial quenching, then rising above the GaN peak, and then quenching again. However, there were quite a few differences from the previous chemically deposited case. For one, there was only one temperature for which increase in intensity was observed, at 400°C. All the other spectra were below the clean GaN spectra. Also, the peak positions this time were quite different from the previous case. The new peaks were observed to appear at 412 nm, 435 nm, and 459 nm. The area under the peaks increased again as expected, though it seemed that the increase in area was much more than the previous time.

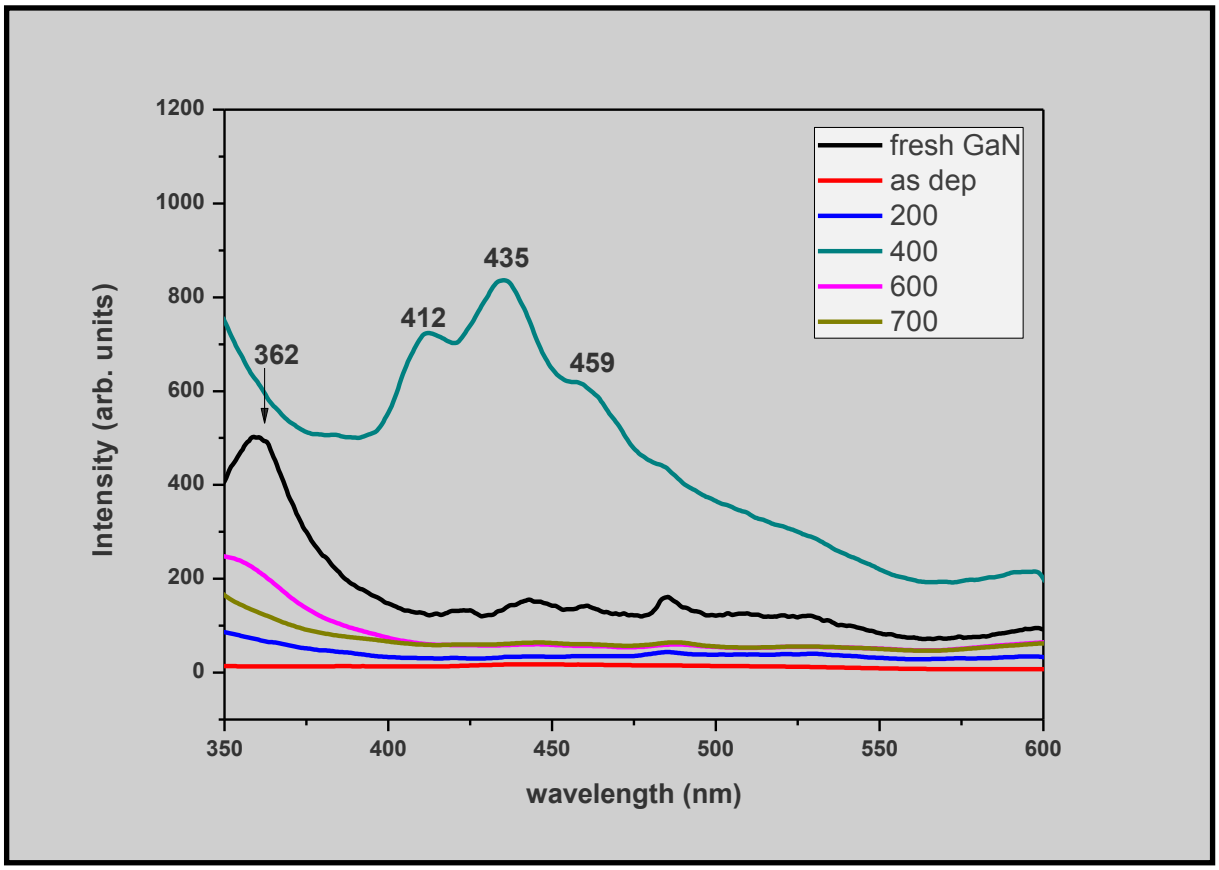

Fig.19 *Photoluminescence spectra of the PVD grown samples – annealing effects shown*

At every annealing temperature, the average particle size was calculated and the corresponding photoluminescence peak intensity was plotted against it. The graph shown below (Fig.20) has temperature on the x-axis, the average particle size on the y-axis with the peak intensity on the alternate y-axis. In the physically deposited samples, the average particle size hardly changes by much, with a range of about 20-110 nm, but it is only at a very narrow range (30-40 nm) is a substantial increase in intensity noted. This denotes a much finer control over the increase in intensity than for the chemically deposited case, where the particle size for which intensity increases remains for a much larger range of temperature. This is immediately observed by the other results, such as SEM, where it can be seen that the average particle size for chemically deposited samples is much larger than it is for physically deposited case. Hence, even when the temperature is increased from 400°C to 600°C, the intensity increases further.

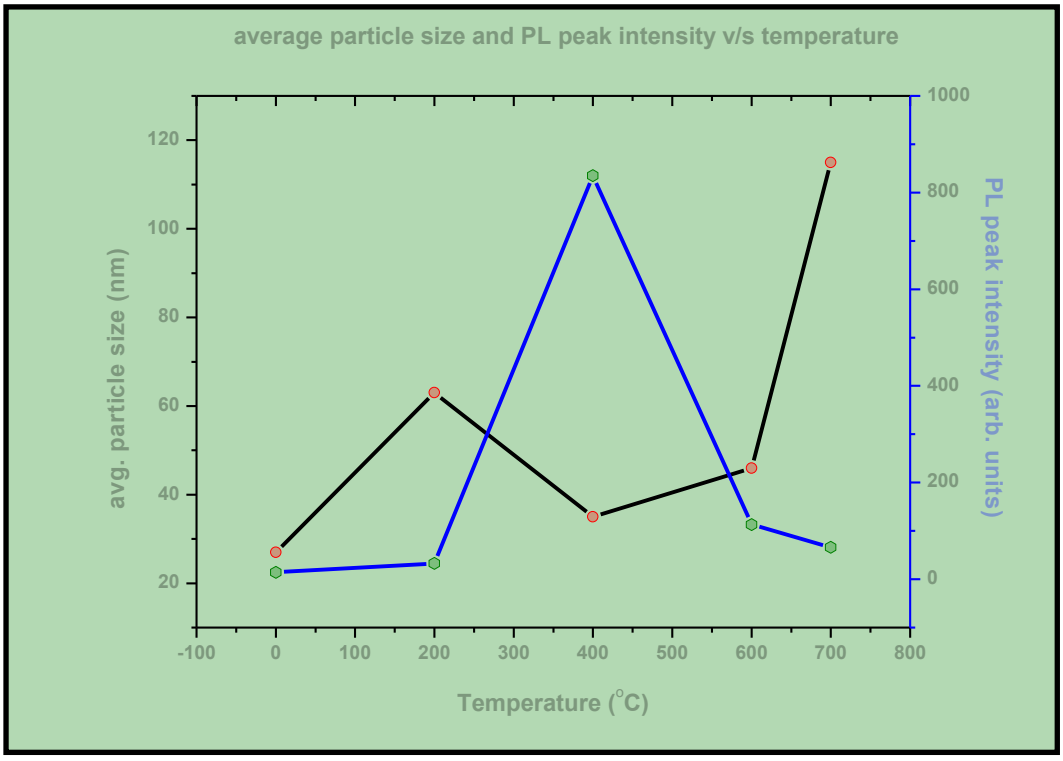

Fig.20 *Comparison between average particle size and peak intensity with temperature*

Comparison between chemical and physical route:

With the same experiment done in two ways, the major characteristics were then compared.

Chemical Route	Physical Route
1. Silver grows mainly as islands	1. Silver grows uniformly as a film over the substrate.
2. Average particle size is 100-600nm with island size extending in microns.	2. Average particle size varies from 1-100nm. There are no large islands.
3. Photoluminescence enhancement shown for a range of temperatures from 400-600°C.	3. Photoluminescence enhancement shown at only 400°C.
4. Extra peaks in the PL spectra observed at 367, 382 and 398nm.	4. Extra PL peaks observed at 412, 435 and 459nm.
5. XPS shows a very small silver peak for medium coverage which increases with annealing.	5. XPS shows a very high silver peak for all samples. The intensity does not vary much with annealing.

A.3.3.3 Flat GaN:

To observe the effect of the nanowall network structure on the experiments, another experiment was carried out - adsorption of silver on a flat (epilayer) GaN surface. Physical route was used to grow silver in this case, and coverage of 1.3 nm, similar to the physically coated network structure, was coated. Annealing was also done at the same temperatures for same time. It was observed that the optical effects seen in the network structure were not repeated when the same experiment was carried out on a flatter surface. Also, silver was observed to be sticking quite less on the surface, which was proved by EDX mapping, and that it completely desorbed upon annealing at 600°C. This shows that the

adsorption of Ag on c-plane is much lower as compared to the nanowall network, which are thought to be dominated by the m-plane of GaN.

Characterization:

(1) Photoluminescence:-

The PL spectra were taken under the same conditions as before. Here, one can see that even though there is a peak associated with silver-GaN coupling at 382 nm, there is no evidence of the effect after annealing. Also, at no point does the intensity cross that of fresh GaN peak. This means that the silver may have been of the proper size and that its interaction with the GaN surface could have been sufficiently strong to give a coupling peak at 382 nm, but the effect is not strong enough to increase that of fresh GaN. Hence, the coupling effect is quite weak in this case. Since annealing leads to no further enhancement in the spectra, one can safely say that such a surface is not suitable for observing the effects of surface plasmon-exciton coupling between silver and GaN.

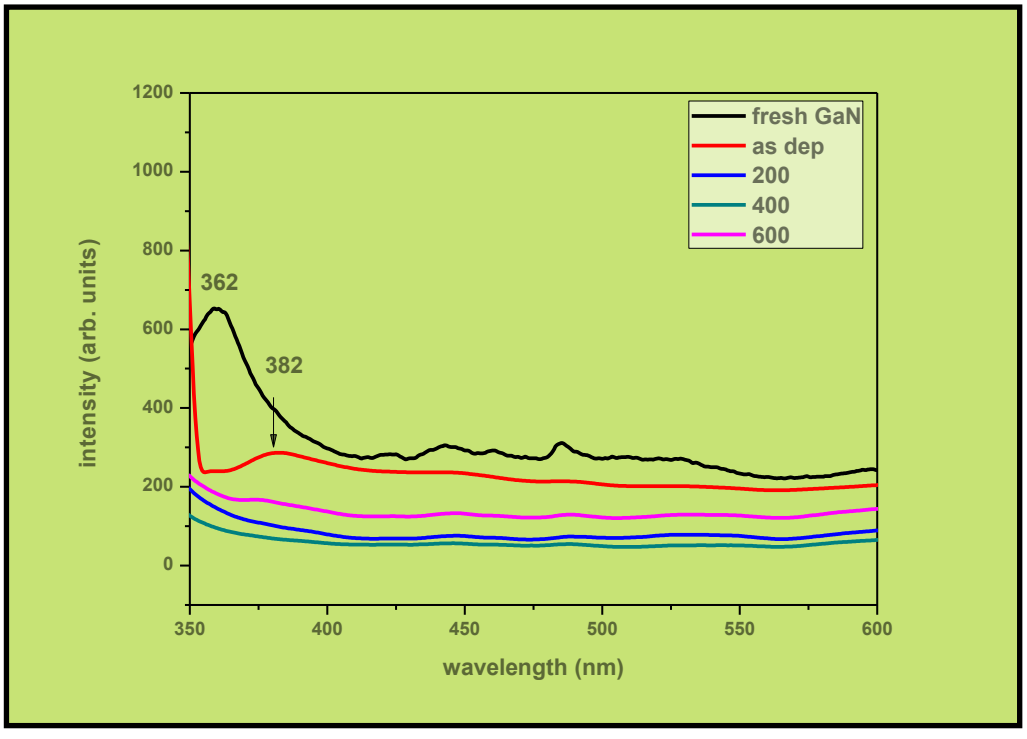

Fig.21 *PL spectra of GaN epilayer – annealing effects shown*

(2) SEM:-

The SEM image was taken on the flat GaN surface after depositing silver for the same time as for the physically-grown sample on GaN nanowall-network. The image shows just a chunk of silver on the surface, leading to the belief that whatever silver got deposited on the surface coagulated to form a big island. Unlike the islands seen in the case of chemically grown samples on the network, this island looks more like a large cluster of silver rather than silver particles coming and coagulating on the surface. This means that silver deposited on a flat surface easily diffuses and the smaller particles coagulate to form one single moiety, and that no particle is large enough to be seen as it is. The latter part is to be expected, since physically grown methods do not give particles as large as islands. However, the property of silver diffusing along the surface is quite surprising, since at this point no external force (e.g. temperature) was provided for it to gain the momentum for such an action.

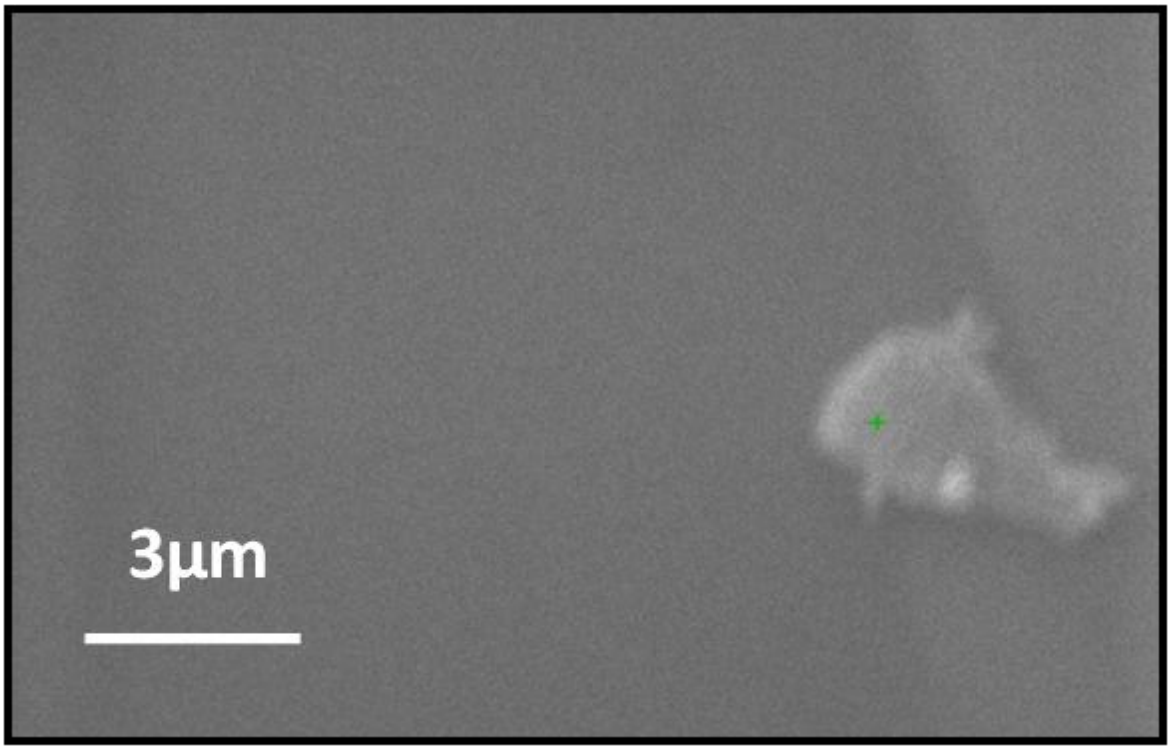

Fig.22 *SEM image of silver as-deposited on flat GaN*

(3) EDX:-

The EDX pattern and quantification were taken under the same conditions as before. The surface shows a richness of gallium, with a Ga:N percentage being 68:27. Silver was present at a good percentage of 2.63, but this could be due to the large chunks present on the surface.

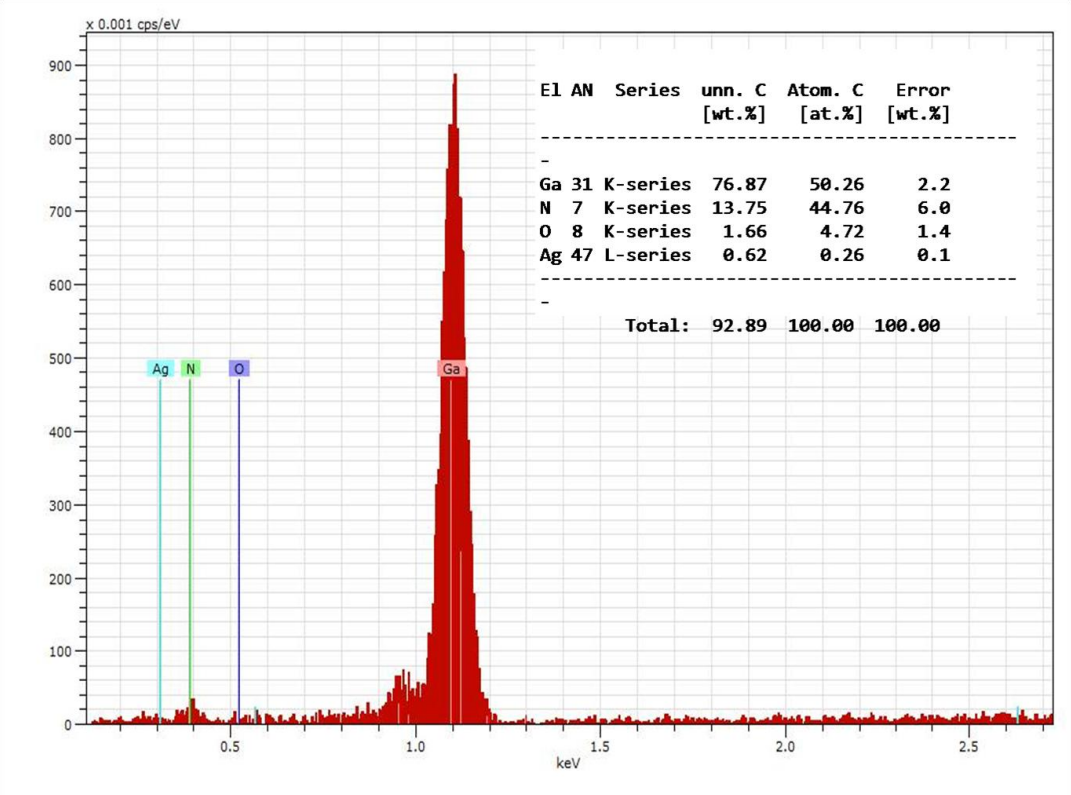

Fig.23 *EDX pattern with quantification shown as an inset.*

(4) Elemental mapping:-

From the elemental maps taken on this surface, it was clear that the amount of silver was quite less compared to Ga and N. Fig. 24 shows the elemental map of the flat GaN, compared with that of network GaN. Fig.24 (a) shows the deposition of silver on the surface. It is

apparent that silver deposits as small particles all over, but is too small to be of any significance to the present study. One large chunk of silver is visible, which is probably due to the coagulation of particles which managed to diffuse along the surface and agglomerate. Fig. 24 (b) shows the relative amounts of Ga and N as compared to silver. Apart from the big chunk, silver is hardly seen on the surface when compared to Ga and N. Fig.24 (c) shows the mapping of silver deposited on network sample as a comparison. It is evident that silver deposits a lot well on the rougher surface.

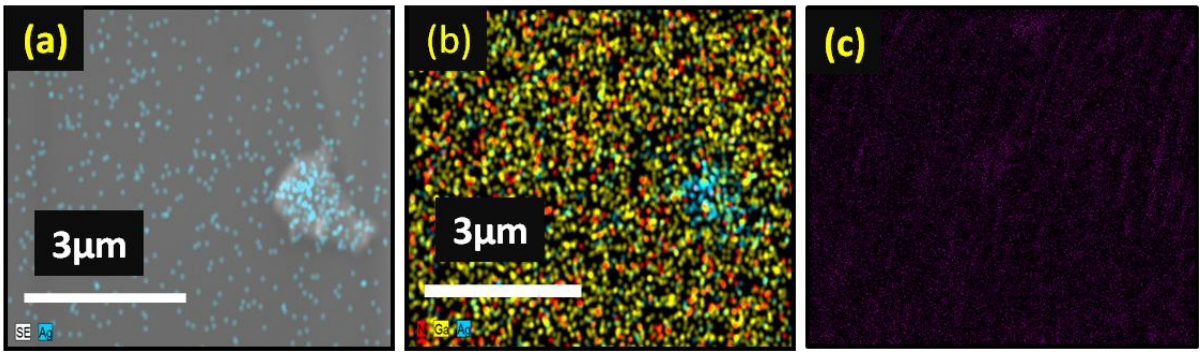

Fig.24 *SEM mapping of Ag deposited on GaN. (a)Silver and the SEM picture of flat GaN overlapped with one another (b)mapping of Ga, N and Ag on flat GaN shown together (c) mapping of silver on the network structure of GaN shown.*

A.3.4 Discussion:-

The photoluminescence results from the three experiments are shown in Fig. 25, with the GaN spectra given for comparison. It can be seen that the observations made previously are all justified in this combined graph, where the spectra of flat GaN dips way below that of the band edge emission.

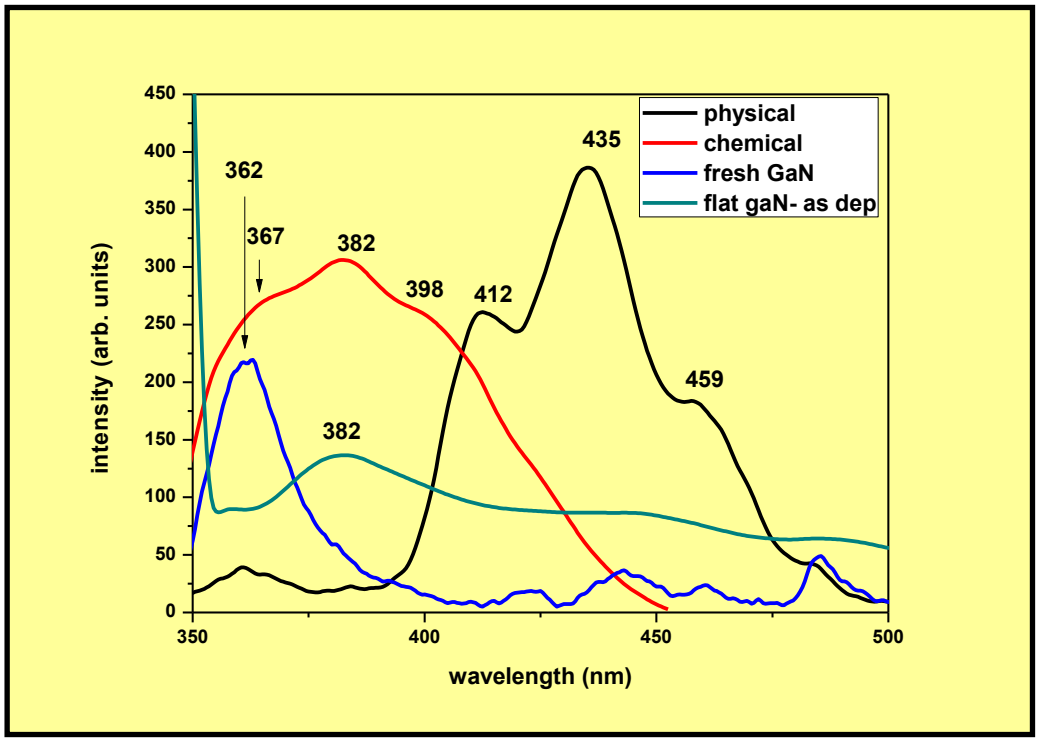

Fig.25 *Photoluminescence results of three experiments compared – high and medium coverages of chemical route and medium coverage of physical route*

A reasoning as to why there were extra peaks observed in the PL spectra for every experiment, we consider the plasmon-exciton coupling between silver and GaN. Silver is known to have the highest quantum efficiency among all the noble metals which exhibit SPR in the visible range. The surface plasmon energy of silver at GaN interface is 2.9eV (~428 nm). As mentioned in the introduction, a lot of work has been done in this area of Ag-GaN coupling, so the effect is not unknown. The interesting point to note here is the fact that the flatter film does not give the increase in intensity which a rougher film does. It could be due to the increased surface area of GaN in the rougher surface and also the rougher surfaces are m-plane GaN, which brings about this effect to be observed so strongly. This hints towards the fact that one can use such kind of surfaces for increasing the emission range and intensity as alternate to making quantum well structures that are at present used to get this effect.

Taking a step by step approach to the observations, the following inferences can be made – when silver covers the surface completely, the band edge emission from GaN is completely deflected, leading to a complete quenching of the spectra. This is known from literature that if the size of the silver is too big or too small, a deflection of emission takes place. However, when we start annealing the sample, the silver either breaks up into smaller particles, like in the chemical deposition case; or it agglomerates due to Oswald ripening, as was observed in the physical case. Then, the emission starts increasing, due to more particles coming into the range of providing the necessary coupling for an enhanced emission to take place, rather than quenching. This leads to extra peaks being observed in the spectra, due to more states being formed in the band gap region. From the different types of deposition observed in the chemical and the physical case, the extra peaks come either nearer to the band edge emission of GaN or near the SPR of Ag. Why the peaks come nearer to the band edge emission of GaN or to the SPR of Ag is probably based on the average size of the silver particles. The smaller the average particle size of silver, the energy transfer is more towards the metal, and the emission is closer to the SP energy of silver. If the average particle size is bigger, though, the emission is closer to the band edge of GaN.

To understand the observations more completely, a model is proposed below, which explains the processes schematically. Since the chemical and the physical route follow a slightly different pattern, a different model is proposed for each of them. For the chemical route, it is:

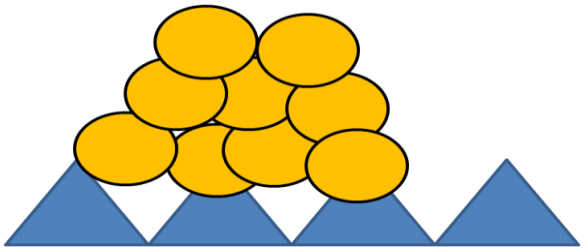

(a)

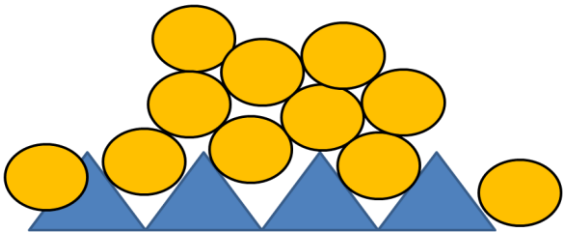

(b)

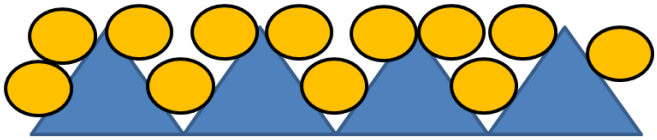

(c)

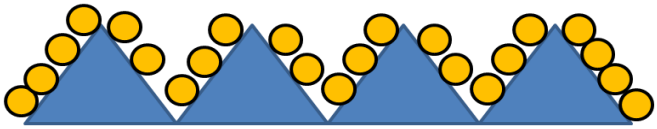

(d)

(e)

Fig.26 *Schematic diagram for chemical deposition case: (a) as deposited islands on top of walls, (b) islands breaking up and individual particles forming, (c) particles depositing on the sides of the walls, (d) particles covering the walls, (e) thin film of silver wetting the walls*

In this model, the whole process has been summarized schematically: (a) demonstrates how the silver initially sits on the GaN surface, being too large, they sit as large particles on top of the walls. The image shows one such agglomeration. With annealing, the particles break up into smaller entities, which are shown in (b) and (c). This is a clear reflection of the observations made earlier in the chemical deposition case. The last figure, (d), shows the eventual status of the system, with silver completely wetting the surface.

For the physical case, one can similarly give a model for the observations made. Since these observations do not follow a similar course as the chemical deposition, difference in the model is required. This time, the process starts with a thin coating of silver being formed all along the walls (Fig.27 (a)), instead of a large cluster on top of them, as was the case in the chemical deposition case. Agglomeration of particles and Oswald ripening occurs in (b) and (c) as silver diffuses along the walls and starts forming islands. Next, the formation of large clusters is shown in (d), which pertains to the situation after annealing to 600°C. The final image is the same as for the chemical deposition model, showing a complete wetting of the surface.

Therefore, from the two models presented for the chemical and physical deposition of silver on GaN nanowall network structure, we conclude that although the starting stage of the chemically and the physically deposited samples is quite different, both of them end up with the same final stage, i.e. wetting the surface.

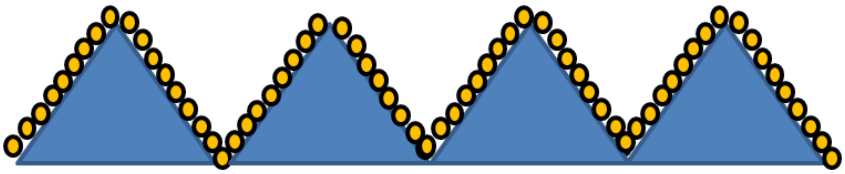

(a)

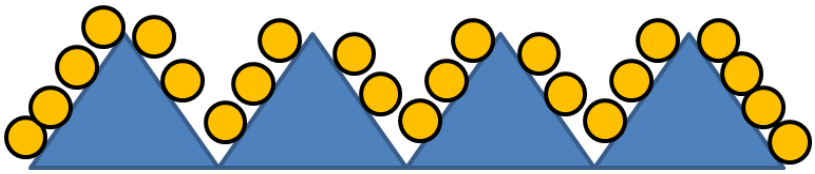

(b)

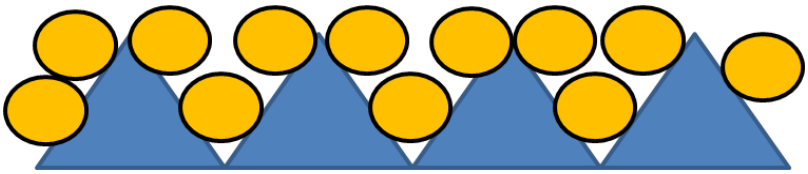

(c)

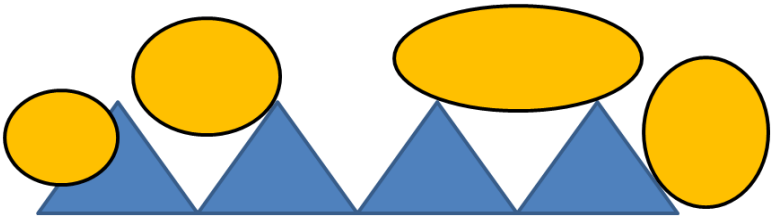

(d)

(e)

Fig.27 *Schematic diagram for physical deposition case: (a) as deposited silver forming a thin layer, (b) islands forming along the walls, (c) Oswald ripening making the islands bigger, (d)large islands, (e) thin film of silver wetting the walls*

A.3.5 Conclusions:-

- Silver could be successfully deposited on GaN surface via both chemical and physical means.
- The nanowall network structure with m-plane walls is better to deposit silver on since on a flat c-plane surface, silver does not stick very well.
- Chemical deposition of silver mainly led to the formation of islands, while a physical deposition gave a uniform coverage.
- The deposited silver was amorphous in nature, since no sign of crystallinity was observed.
- Annealing led to the formation of smaller islands, both in the case of chemical as well as physical deposition.
- Optical studies indicate that annealing leads to increase in the interaction of silver with GaN, and at some particular temperature, this interaction becomes so high that an increase in the intensity of the photoluminescence spectra is seen. For chemically deposited silver samples, this occurs at more than one temperature, while for physically deposited samples this happens at only one temperature.
- The surface of the GaN seemed to become metallic after depositing silver, which was observed via valence band measurement in XPS. A non-zero density of states at Fermi level confirms that the semiconducting nature of the GaN was replaced by a metallic one.

A.3.6 Extra work attempted:-

Below are mentioned some of the other studies done on the same system, but since conclusive results were not obtained, they are not presented in this thesis.

1. AFM image of polymer (PDMS) coated on GaN – making of a mask
2. SERS measurements on silver-coated GaN – enhancement observed
3. I-V measurements to show linearity with silver observed, Hall measurements to calculate carrier concentration, mobility.

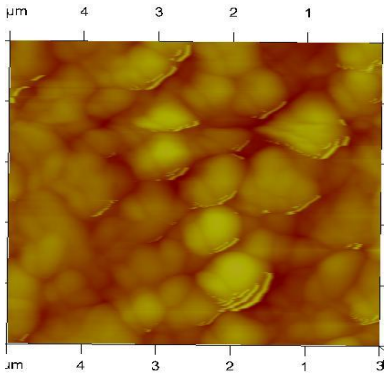

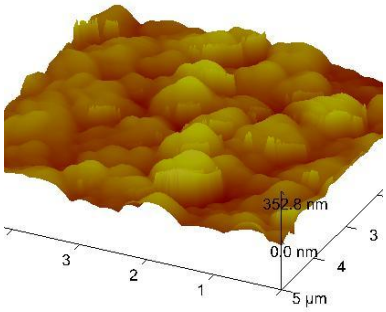

PART B

Experimental & Theoretical Analysis of co-adsorption of CO and Ni on Ru (0001) surface

Chapter B.1
Introduction

One of the major goals of surface science has been to develop a fundamental understanding of the reactivity of transition metal surfaces [45-48]. Such an understanding, if realized, could potentially provide concepts for the interpretation of kinetic data on heterogeneous catalysis. However, catalytic systems are too complex for such theories to develop.

Alloy catalysts are very promising candidates for the improvement of rate and selectivity in a variety of catalytic reactions [49-51]. In this context, it is important to understand and control the reactivity of metal-on-metal structures that serve as model systems. Here phenomena such as epitaxial growth and surface alloys offer the opportunity to construct structures that are not otherwise found in nature. Already, a quite detailed picture of the electronic factors determining surface reactivity has been established [52]. Hereby, the astonishing correlation between the core level shift and the CO chemisorptions energy found for a number of both pristine metal surfaces and overlayer structures [53] can be rationalized. Using density functional theory (DFT) calculations it was shown that the position of the d-band centre determined the CO chemisorption energy [54]. Future research should exploit this detailed knowledge in the design of novel materials for heterogeneous catalysis.

B.1.1 Epitaxial growth: The term epitaxy is derived from the Greek words *epi*, meaning "above", and *taxis*, meaning "in an ordered manner". Hence, epitaxy refers to a method of growth where one film grows on top of another in an ordered manner. By "ordered manner" one usually refers to some kind of geometrical relationship between the substrate and the overgrown film. In general, both the substrate and the overlayer used in epitaxial growth are monocrystalline in nature.

Epitaxial films can be grown from gaseous or liquid precursors. The substrate acts as a seed for the overlayer; and hence the overgrowing film takes on the lattice structure and orientation identical to those of the substrate. Such a phenomenon is commonly known as "pseudomorphic growth". The pseudomorphic growth generally lasts for a few layers after which the material growing on the substrate takes on its own lattice parameter. This is understandable because in a pseudomorphic growth situation, the overlayer is under a strain, which may be either tensile or compressive, depending on the difference in the unit cell sizes of the substrate and the overlayer. After a few layers, when the substrate effects diminish considerably, the strain also reduces and finally a film of the overlayer with its own lattice parameter is obtained. If the film and the substrate share the same composition, the process is called homoepitaxy, else it is known as heteroepitaxy.

There are certain conditions as to how a film grows on top of another substrate; if the lattice mismatch between the overlayer and the substrate is too less, then the overlayer adopts the lattice parameter of the substrate and grows as a flat film. However, if the lattice mismatch is too much, then the overlayer, growing pseudomorphically at first, quickly adopts its own lattice parameter and grows as islands on the substrate. There is another way for the film to grow, which is a mix of both island and flat film. If the lattice

mismatch is not too low or not too high, then the film would initially grow as islands, but would form flat films later. This procedure would be repeated a few times until there are enough layers of the film formed on the substrate so that the overlayer can grow as a flat film.

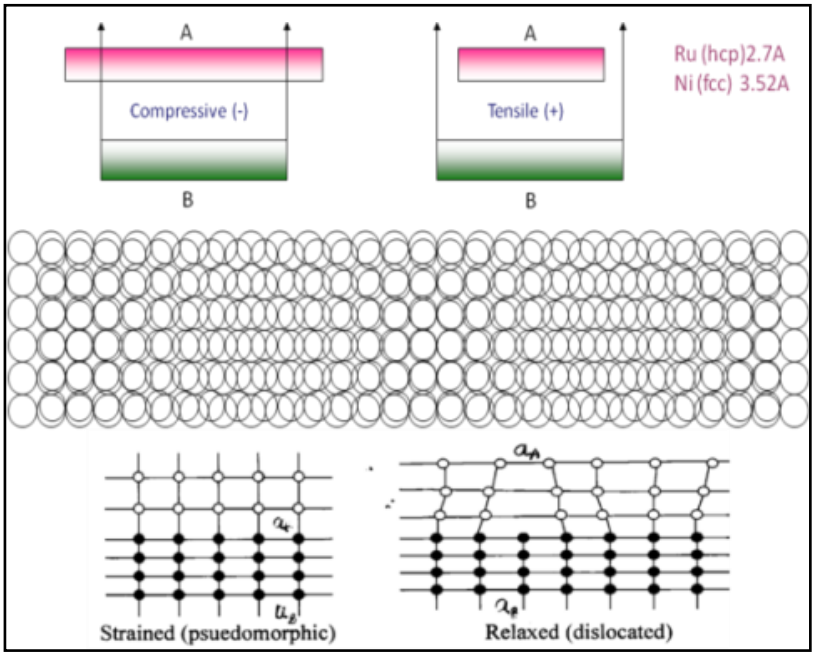

Fig.1 *A schematic diagram showing pseudomorphic and relaxed structures. Two types of stress that occur due to lattice mismatch are also depicted*

B.1.2 <u>Growth modes:</u> The growth of epitaxial thin films on a single crystal surface depends strongly on the interaction strength between the adatoms (atoms of the overgrowing film – short for adsorbed atoms) and the surface. Although it is possible to grow epilayers (short for epitaxial layers) from a liquid solution, mostly a vapour phase method such as molecular beam epitaxy (MBE) is used for the purpose. Three major types of thin film growth modes are known: 1) Volmer-Weber (VW) growth, 2) Frank-van der Merwe (FM) growth, and 3) Stranski-Krastanov growth.

1) Volmer Weber (VW) growth mode – In a VW type of growth, the interactions between the adatoms are stronger than the interactions between the adatoms and the surface, leading to the formation of three-dimensional adatom clusters, or islands. For this reason, VW type of growth is also called an island type growth. These clusters, along with coarsening, cause multi layer films to grow on the substrate surface.

2) Frank-van der Merwe (FM) growth mode – In this case, the interactions of adatoms are stronger with the surface than with each other. This leads to atomically smooth, fully formed layers. A two-dimensional layered growth takes place, indicating that a complete coverage by one layer takes place before the next layer starts to grow.

3) Stranski-Krastanov growth mode – This is an intermediary process where both a 2-D film and a 3-D island growth is observed. At a critical layer thickness which is highly dependent on chemical and physical properties like surface energies and lattice parameters, a transition from layer-by-layer to island growth takes place.

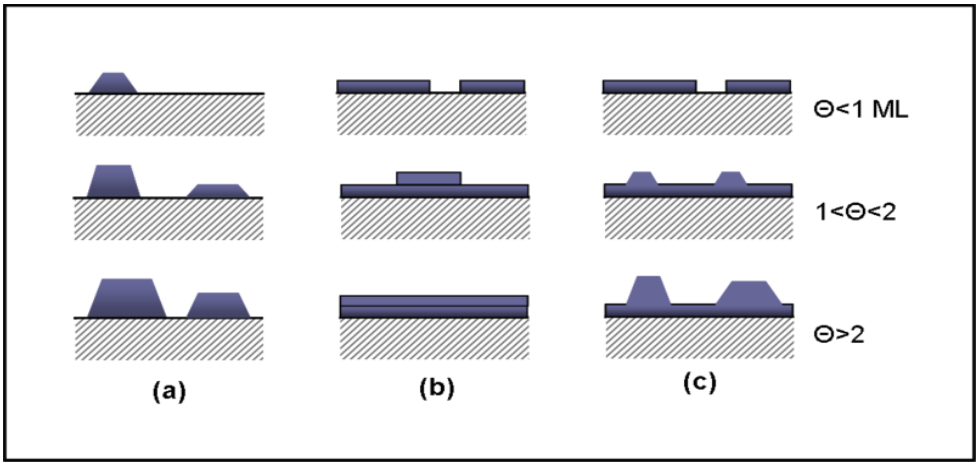

Fig.2 *Three types of growth modes shown: (a) VW or island type, (b) FM or layer-by-layer type, and (c) SK, the combination of both island and layer-by-layer growth*

B.1.3 CO-Nickel-Ruthenium system:-

Carbon monoxide adsorbed on Ruthenium is a fairly well known system. Many structural aspects of related work have been reported in the past [55-58]. The interactions between molecules and metal surfaces is of great interest in surface science since key physical and chemical properties can be described by such systems, such as energy transfer and molecular reactivity, extremely useful in, e.g. catalysis.

The catalytic properties of Ni/Ru(0001) have also been widely discussed in literature. The study of how the chemical reactivity of ruthenium surface changes when nickel has been adsorbed over it has given a new direction in the study of catalysis on metal surfaces [59, 60].

Here, the system that has been considered involves nickel growth over ruthenium with pre-adsorbed carbon monoxide. The structural changes in the nickel layer have been studied with adsorption of carbon monoxide molecules and this has helped in understanding the changes that occur when carbon monoxide is exposed to a metal layer.

Chapter B.2

Experimental Motivation

The work presented here is motivated by an experiment, which dealt with the study of formation of nickel islands on ruthenium, with CO pre-adsorbed.

B.2.1 Summary of the experiment:

In this experiment, ruthenium (0001) surface was taken and was exposed to CO. Next, growth of nickel atoms was studied on these ruthenium surfaces. As a control, nickel growth on bare ruthenium substrate was also studied.

B.2.2 Results and discussion:

Upon adsorbing nickel on ruthenium after the ruthenium substrate had been pre-adsorbed with CO, it was found by high resolution STM studies that nickel formed islands on ruthenium (Fig.1). The growth mode of nickel was identified to be VW type, since islands were observed to form all over the Ru surface.

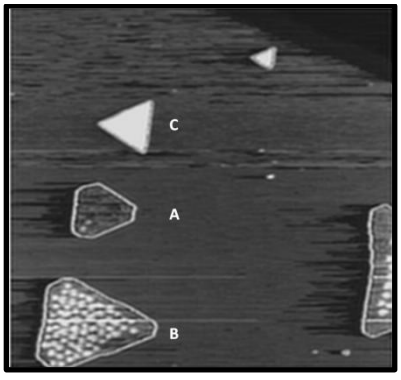

Fig.1 *Island growth of nickel on ruthenium substrate. Three types of islands are observed, with A and B showing pseudomorphic growth and C showing a reconstructed growth. The white colour represents atoms which are at a higher level*

Three types of islands were observed: A is the nickel forming a pseudomorphic layer over ruthenium. From the figure, it is apparent that the height of this island is about the same as that of the substrate. The corners of the islands are also quite blunt, meaning that the formation of the island is not very precise, but a function of the dislocations arising due to lattice mismatch. In the second type of island B, there are white spots visible. This means that there are some atoms higher than others, which causes the colour difference in the image. However, C shows a completely different behaviour than A and B. It can be seen that C type of islands pointed opposite to the A and B type, and the corners were sharper. Also, the C type islands are completely white, indicating that all the atoms in this island were higher than the substrate.

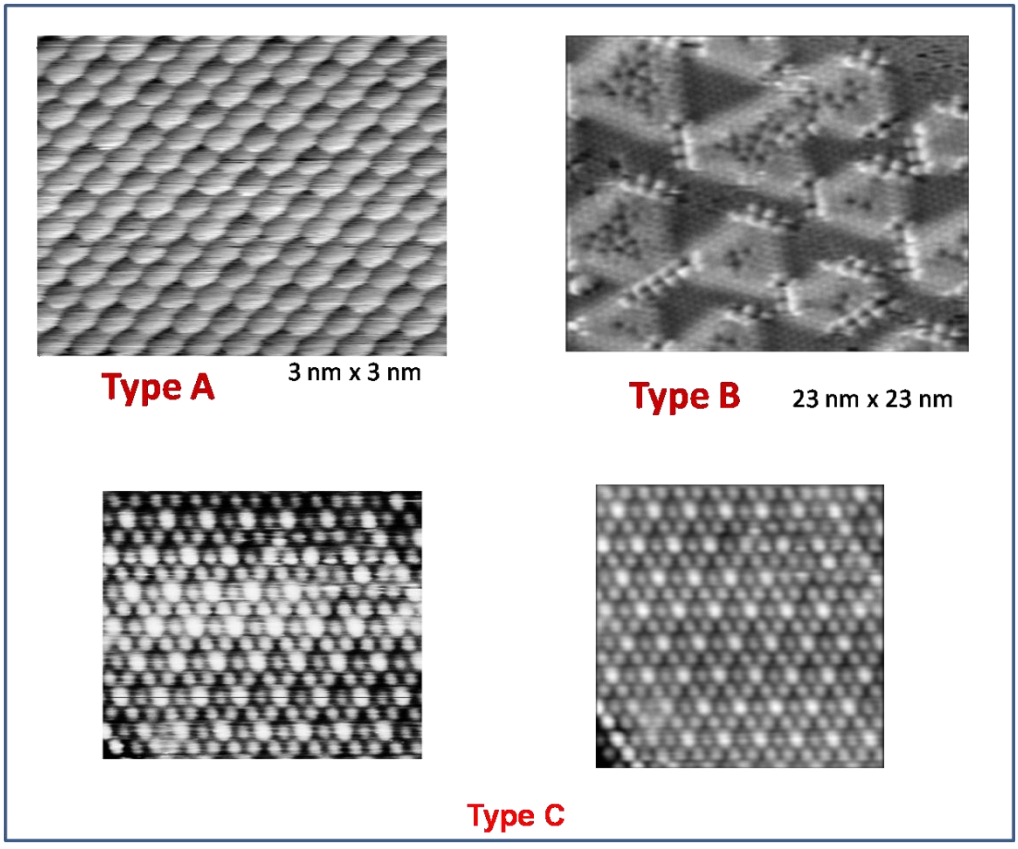

Fig.2 *A zoomed in image of the three types of islands observed: a shows a completely pseudomorphic growth, B shows atoms moving about with reconstruction taking place; three different heights of atoms are clearly visible. C shows a picture quite different from A and B, it is a completely reconstructed image*

A zoom-in to the three types of islands made the initial observations clearer. The structural differences between the three types of islands are shown in Fig.2. 'A' type islands can be seen growing the same way as the substrate, i.e. a pseudomorphic growth is taking place and the nickel is also growing in the hcp sites as the ruthenium. All the atoms are in the same plane, i.e. no height difference is observed. In the case of B, atoms are mainly at three different heights. This indicates that there is a reconstruction taking place. The triangular shaped islands show black coloured atoms in their centre, lighter coloured atoms at the edges and completely white atoms at the outer part of these edges. From these images, it was concluded that atoms on the edges of triangles are on the verge of transiting from hcp to fcc sites, while the white atoms are the ones sitting on fcc sites. The C type islands were only observed when the surface was pre-adsorbed with CO. Since CO was absorbed on the surface in patches, the C type islands were also found scattered along the surface, rather than being uniformly distributed. Also, the atomic arrangement was completely changed. This indicated that the reconstruction took place from B to C. The atomic arrangement of C type islands, shown in Fig.2, indicates that most of the atoms are in fcc sites, which causes the island to look completely white in a STM image. However, a closer observation shows that the atoms are at three different heights in these islands, indicating that a reconstruction is occurring similar to B type islands. To explain why the atomic structure of a C type island is different from a B type island, a model of quartet reconstruction was proposed (Fig.3).

In the quartet reconstruction model, the atoms were treated as groups of four, as indicated by the STM image. One of the atoms was adsorbed on a hollow site, while the other three atoms were pulled towards it. In the figure, the D atom is considered to be present on a hollow site, while A and B are on the bridge sites. The C atom is on an "on top" site. When these three atoms, A, B and C, move towards D, the atoms A and B move

equal distances, causing the increase in their heights to be the same. The C atom is the one that goes over an atom in order to come closer to the D atom, causing its height to be increased by maximum. Hence, we get three different heights from the model: the C being the highest, A and B being lower than C but higher than D, and D being the lowest in height.

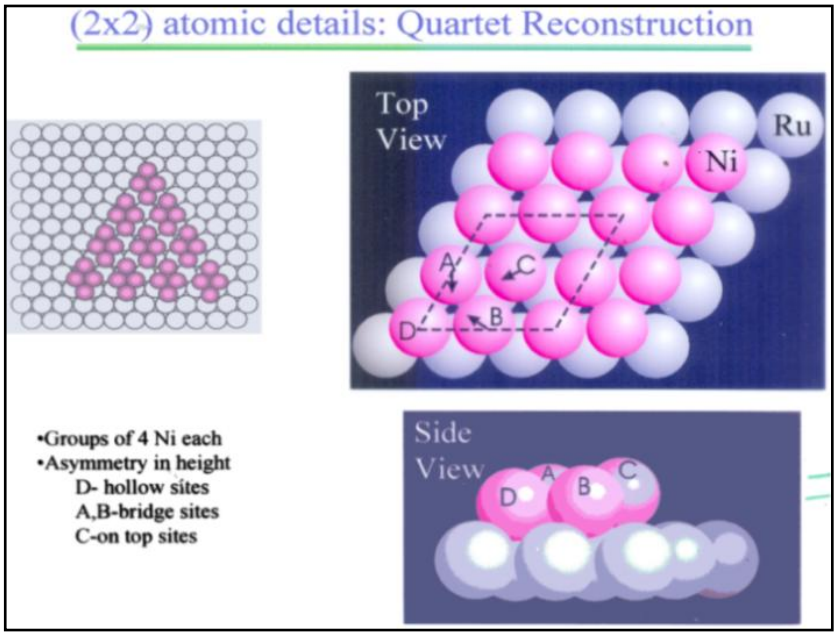

Fig.3 *Proposed model for the reconstruction of the nickel layer. The quartet term comes from the fact that atoms are considered in groups of four*

An explanation was also suggested for why the atoms in C type islands were sitting in fcc sites rather than hcp sites; the carbon monoxide molecule is believed to rotate so that it blocks the hcp sites and the incoming nickel atoms are forced to sit in the less favourable fcc sites (Fig.4). This is what is called the quantum rotor model, since the CO molecule rotates while sitting on top of nickel.

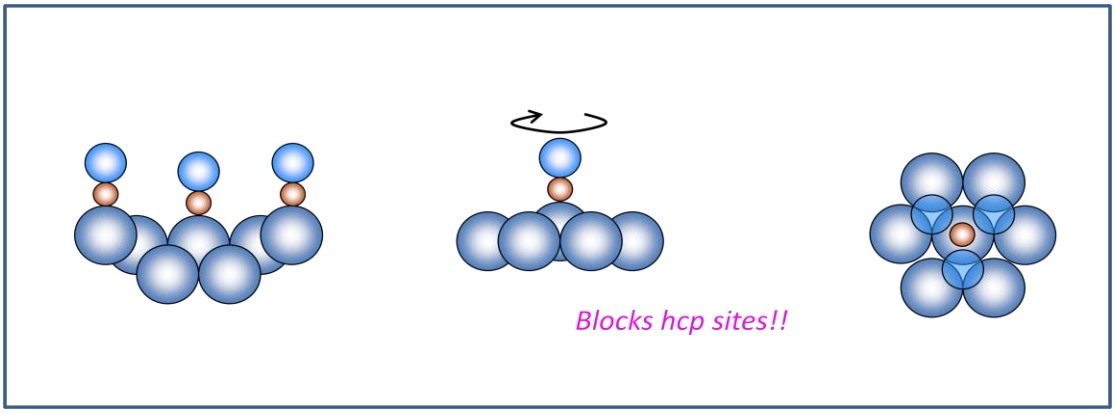

Fig.4 *A model to show that the CO molecule sitting on top of nickel rotates to block the hcp sites nearby*

Fig.5 shows the growth of nickel islands on ruthenium steps. Each step is aligned opposite to the previous, which explains why the edges of the steps are different. The corrugated edges signify the direction in which nickel islands grow. Consider the corrugated step in the figure. The direction of the corrugation is towards the left. Therefore, all nickel islands formed on the left of this step should point to the left if they conform to the surface direction. Such nickel islands are in hcp sites. However, some nickel islands are still observed which point opposite to the general direction. This means that those nickel islands are growing in fcc sites.

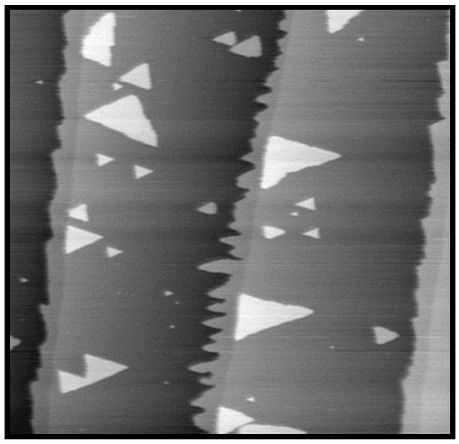

Fig.5 *Nickel islands growing on Ruthenium terraces. Alternating corrugated and smooth step edges can be seen. The nickel islands grow on the step edge, and hence have either pointed edge outward or the flat edge outward*

B.2.3 Conclusions:

- Nickel islands were observed to grow differently on bare ruthenium surfaces and on ruthenium surfaces pre-adsorbed with CO.

- On bare ruthenium, nickel grew pseudomorphically on hcp sites and with more coverage, a reconstruction was observed to start.

- Wherever CO was adsorbed, nickel islands grew in the fcc sites of ruthenium. Atomic images showed the reconstruction occurring in a different way.

- Quartet reconstruction model was suggested to explain the height differences observed in the atomic images of nickel islands growing on ruthenium surfaces pre-adsorbed with CO.

- To explain the reason why nickel was exclusively adsorbed in fcc sites of ruthenium, a quantum rotor model was proposed.

Chapter B.3

Theoretical Studies

Method used – **Density Functional Theory**

B.3.1 Introduction:

The density functional theory (DFT) is an extremely successful approach to describe the ground state properties of materials. DFT can not only be employed to study bulk materials but also proteins and carbon nanotubes. The main idea of DFT is to describe a many body problem by its spatial density. Then, for a system of N particles, which would otherwise have 3N degrees of freedom and hence as many coordinates, the problem reduces to just three coordinates in DFT.

The basis of DFT is given by two theorems, called the Hohenberg-Kohn theorems [61]. The first theorem states that the ground state properties of a many electron problem are uniquely determined by an electron density that depends on 3 spatial coordinates. The second theorem defines an energy functional (functions of functions) for a system and proves that the ground state energy is the minima of that energy functional.

Using these two theorems, DFT writes an eigenvalue equation for the N-particle wavefunction in such a way so as to reduce it to one in terms of energy density $\rho(\mathbf{r})$, which depends on three variables [62]. Hence, the total energy E of the system is written as a functional of the charge density:

$$E[\rho] = T[\rho] + \int V_{ext}(\mathbf{r})\rho(\mathbf{r})d\mathbf{r} + V_H[\rho] + E_{xc}[\rho]$$

Where T is the kinetic energy of the system and V_{ext} is the external potential acting on the system.

DFT has been popularized for calculations in the field of solid state physics since the 1970's due to its fine agreement with experimental observations. Later, the approximations used in DFT were refined even more to better model the exchange and correlation interactions, which made DFT extend into the domain of quantum chemistry.

Despite its many advantages, there still are many difficulties in using density functional theory to properly describe intermolecular interactions, especially dispersive forces such as van der Waals' interactions. Research is being done to further improve DFT so as to remove such drawbacks.

In the theoretical calculations, the package used is Quantum Espresso version 4.0.1 [63]. The pseudopotentials [64] for various atoms are as follows: Ruthenium- Ru.pbe-n-van.UPF, Nickel – NisrPBE.RRKJ3.UPF, Carbon- C.pbe-van_bm.UPF and Oxygen- O.pbe-van_bm.UPF. Kinetic energy cutoff for the wavefunctions was at 25 Rydberg, and a k-point mesh of 4x4x1 [63] was used.

B.3.2 Results and Discussion:

One layer of nickel was adsorbed over five layers of ruthenium atoms. First, nickel was put in hcp sites (Fig.1). Freezing the bottom two layers of ruthenium

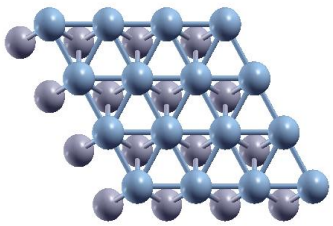

Fig.1 *Ni adsorbed on hcp sites of Ru*

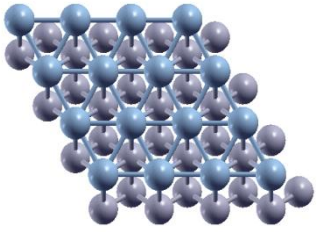

Fig.2 *Ni adsorbed on fcc sites of Ru*

(considering bulk), the atomic layers above were relaxed and the energy of nickel in hcp site was calculated to be -4.6494 keV.

Again, taking the same structure but putting nickel in fcc sites this time (Fig.2), the energy was calculated and it came out to be -4.6493 keV. The difference in energies was calculated to be 0.1eV, which was quite significant. Hence, further calculations were done taking nickel in the fcc site.

Taking Ni adsorbed on hcp as starting point, CO was adsorbed on the on-top sites of Ni, in a unit cell of 2x2 (Fig.3) as well as √3x√3 (Fig.4), relaxing of the atomic layers above the bottom two showed that the CO molecule pulls the nickel atom below it a fraction above the layer.

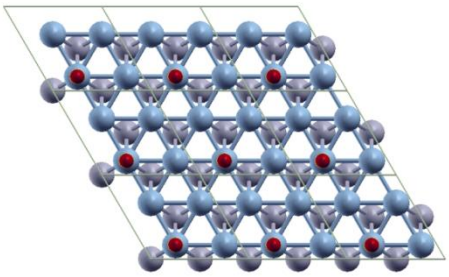

Fig.3 *CO adsorbed on top of Ni in a 2x2 fashion*

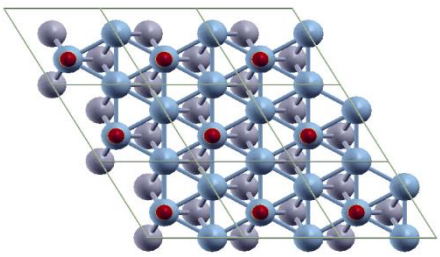

Fig.4 *CO adsorbed on top of Ni in a √3x√3 fashion*

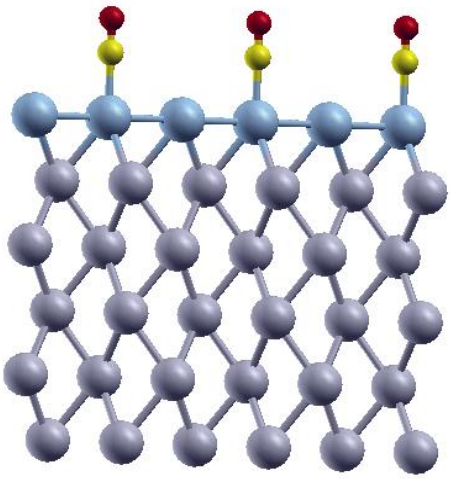

Fig.5 *Side View of the structure: the purple atoms are ruthenium, the blue ones above are nickel, and the yellow and red on top of nickel are carbon and oxygen respectively*

The adsorption energies of CO were calculated in both unit cells by subtracting the energy of only CO from the energy used to adsorb CO, which was calculated by subtracting the energy of nickel on ruthenium from the energy of CO adsorbed nickel on ruthenium. For the 2x2 cell it was calculated to be -1.6638 eV and for √3x√3 cell it was -1.6357 eV.

In the previous calculations, the paramagnetic character of nickel was not taken into account. Hence, the spin of nickel was incorporated as an additional parameter into the calculations and it was found that the new adsorption energies for the 2x2 unit cell rose by about 0.02 eV while for the √3x√3 cell it fell by about 0.03 eV; for the 2x2 cell it was now -1.6489 eV while √3x√3 cell it was -1.6633 eV.

This shows that magnetization plays a role in the determination of adsorption energy. However, it is not very clear as to whether the adsorption energy rises or falls in every case. More studies on the topic may reveal a trend. A simple reason as to why the incorporation of magnetization should affect the adsorption energy is that since CO is adsorbed directly on top of nickel, an unpaired electron in nickel would result in polarization of the CO molecule, and a charge transfer mechanism may take place, thereby affecting its interaction with the nickel atom.

However, there is still more work required to confidently predict about the nature of such interactions and their effects.

The CO adsorbed on the nickel was also rotated to different angles to see if it prefers to sit at any particular angle to the nickel layer (Fig.6). In every case, though, it was found that the CO molecule snaps back to vertical position (~179.87°) at equilibrium.

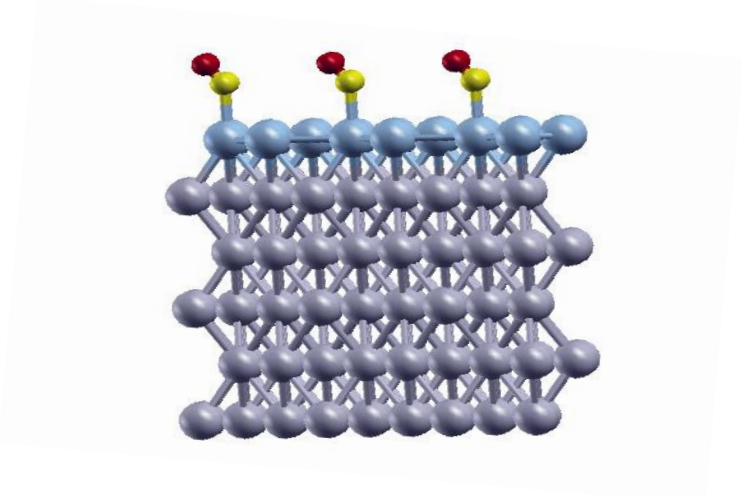

Fig.6 *CO molecule rotated on top of nickel: it would come back to vertical position at equilibrium*

The effect of CO on the Ni-Ru bond length was also studied, both with and without taking into account the spin of Ni, and this further affirmed the observation that there is a definite effect of spin on the adsorption energy of CO.

(a)Without spin

System	2x2 (Å)	√3x√3(Å)
Ni on Ru	2.5484	2.5462
CO on Ni on Ru	2.5363 (for Ni without CO), 2.6289 (for Ni with CO adsorbed)	2.5376 (for Ni without CO), 2.6298 (for Ni with CO adsorbed)

(b) With spin

System	2x2 (Å)	√3x√3(Å)
Ni on Ru	2.5556	2.5513
CO on Ni on Ru	2.5654 (for Ni without CO), 2.6377(for Ni with CO adsorbed)	2.5826 (for Ni without CO), 2.6665 (for Ni with CO adsorbed)

Theoretical studies using DFT as a tool are generally quite robust and reliable methods to give proofs of experiments. However, in this case many results seem to be in direct contradiction to experimental results and also logical intuitions. This means there must be some other parameter missing in this study which the experiment incorporates.

The quantum rotor model and the quartet reconstruction that were suggested based on experimental results could also not be verified by theoretical calculations.

B.3.3 Conclusions:

- The hcp site came out to be energetically more favourable, although by a very slim margin. Still, we took nickel adsorbed on fcc sites for further calculations as experimentally, when CO is adsorbed, nickel is on fcc sites.
- Upon adsorbing CO on top of the nickel, there was a marginal displacement of the nickel atom directly below it.
- CO preferred to sit on nickel in a 2x2 unit cell rather than in a $\sqrt{3}x\sqrt{3}$ unit cell, which was not according to the experiment, since $\sqrt{3}x\sqrt{3}$ was experimentally found to be the favoured unit cell.
- Incorporating magnetization as a parameter in the calculations showed a difference in the adsorption energy, which was to be expected since nickel has one unpaired electron, which polarizes the CO molecule sitting on top of it.
- Rotation of CO molecule to different angles was of no use, as it always returned to an almost vertical position at equilibrium.
- More complex calculations including concepts of a quantum rotor model need to be performed and other growth parameters need to be included in order to mimic the experimental observations made by the STM studies.

References:-

1. Alvarez, M.M. *et al., J. Phys. Chem. B,* **101**, 3706 (1997)
2. Chen, S. and Kimura, K., *Langmuir*, **15**, 1075 (1999)
3. El-Sayed, M.A., *Acc. Chem. Res.*, **34**, 257 (2001)
4. Bouhelier, A. *et al., Phys. Rev. Lett.*, **95**, 267405 (2005)
5. Jensen, T.R., Malinsky, M.D., Haynes, C.L. and Van Duyne, R.P., *J. Phys. Chem. B*, **104**, 10549 (2000)
6. Chao, W-H, Wu, R-J, Tai, C-S and Wu, T-B, *J. App. Phys.*, **107**, 013101 (2010)
7. Cheng, P. *et al., App. Phys. Lett.*, **92**, 041119 (2008)
8. Ritchie, R. H., *Phys. Rev.*, **106,** 874 (1957)
9. Burstein, E., *Polaritons*, 1-4 (Pergamon, New York, 1974)
10. Hecht, B. e*t al., Phys. Rev. Lett.* **77,** 1889 (1996)
11. Pendry, J., *Science* **285,** 1687 (1999)
12. Kneipp, K. *et al., Phys. Rev. Lett.*, **78**, 1667 (1997)
13. Nie, S.M. and Emery, S.R., *Science* **285**, 1687 (1999)
14. Ditlbacher, H., Krenn, J.R., Schider, G., Leitner, A. and Aussenegg, F.R., *App. Phys. Lett.*, **81**, 1762 (2002)
15. Juza, R. and Hahn, H., *Z. Anorg. Allgem. Chem.*, **234**, 282 (1938)
16. Pankove, J. in "*Optoelectronic Properties of Semiconductors and Superlattice*" (O. Manasreh, Ed.) "*GaN and Related Materials*" vol.**2**, p.1. Gordon and Breach Science Publishers, 1997
17. Maruska, H.P. and Tietjen, J.J., *App. Phys. Lett.*, **15**, 367 (1969)
18. Amano, H., Sawaki, N., Akasaki, I. And Toyoda, Y., *App. Phys. Lett.*, **48**, 353 (1986)
19. Amano, H., Kito, M., Hiramatsu, K. and Akasaki, I., *Jpn. J. App. Phys.*, **28**, L2112 (1989)
20. Nakamura, S. and Fasol, G. in "*The Blue Laser Diode*" Springer Verlag, Heidelberg, 1997
21. Mizuta, M., Fujieda,S., Matsumoto, Y. and Tawamura, T., *Jpn. J. App. Phys.*, **25**, L945 (1986)
22. Barski, A., Roessner, U., Rouviere, J.L. and Arlery, M., *MRS Internet J. Nitride Semicond. Res.*, **1**, 21 (1996)
23. Xie, Y., Wang, Y.Q.W., Zhang, S. and Zhang, Y., *Science*, **272**, 1926 (1996)

24. Lada, M., Cullis, A.G., Parbrook, P.J. and Hopkinson, M., App. Phys. Lett., 83, 2808 (2003)
25. Xia, H., Xia, Q. And Ruoff, A.L., *Phys. Rev. B*, **47**, 12925 (1993)
26. Lin, J.M., Lin, H.Y., Cheng, C.L. and Chen, Y.F., *Nanotechnology*, **17**, 4391 (2006)
27. Okamoto, K. *et al.*, *Nat Mater.*, **3**, 601 (2004)
28. Neogi, A. *et al.*, *Phys. Rev. B*, **66**, 153305 (2002)
29. Gontijo, I. *et al.*, *Phys. Rev. B*, **60**, 11564 (1999)
30. Okamoto, K. *et al.*, *App. Phys. Lett.*, **87**, 071102 (2005)
31. Guha, S. and Bojarczuk, N.A., *App. Phys. Lett.*, **72**, 415 (1998)
32. Nakamura, S. *et al.*, *Jpn. J. App. Phys.*, **35**, L74 (1996)
33. Morkoç, H. and Mohammad, S.N., *Science*, **267**, 51 (1995)
34. Kipshidze, G. *et al.*, *J. App. Phys.*, **93**, 1363 (2003)
35. Jani, O., Ferguson, I., Honsberg, C. and Kurtz, S., *App. Phys. Lett.*, **91**, 132117 (2007)
36. Chen, X. *et al.*, *Phys. Stat. Sol. A*, **205**, 1103 (2008)
37. Park, S-H and Chuang, S-L, *App. Phys. Lett.*, **72**, 3103 (2009)
38. Schubert, E.F. *Light-Emitting Diodes* (Cambridge: Cambridge University Press, 2003)
39. Speck, J.S. and Rosner, S.J., *Physica B*, **273**, 24 (1999)
40. Bernardini, F., Fiorentini V. and Vanderbilt, D., *Phys. Rev. B*, **56**, R10024 (1997)
41. Takeuchi, T. *et al.*, *App. Phys. Lett.*, **73**, 1691 (1998)
42. Kwon, M.K. *et al.*, *Adv. Mater.*, **20**, 1253 (2008)
43. Yeh, D.M. *et al.*, *App. Phys. Lett.*, **91**, 171103 (2007)
44. Kim, B.H. *et al.*, *Adv. Mater.*, **20**, 3100 (2008)
45. Somorjai, G.A., *Introduction to Surface Chemistry and catalysis* (John Wiley, New York, 1994)
46. Greeley, J., Nørskov, J.K. and Mavrikakis, M., *Annu. Rev. Phys. Chem.*, **53**, 319 (2002)
47. Larsen, J.H. and Chorkendorff, I., *Surf. Sci. Rep.*, **35**, 165 (1999)
48. Hammer, B. and Nørskov, J.K., *Adv. Catal.*, **45**, 71 (2000)
49. Sinfelt, J.H., *Science*, **195**, 641 (1977)
50. Ponec,V., *Adv. Catal.*, **32**, 149 (1983)
51. Sachtler, W.M.H. and van Santen, R.A., *Adv. Catal.*, **26**, 69 (1977)
52. Hammer, B. and Nørskov, J.K., *Surf. Sci.*, **343**, 211 (1995)
53. Rodriguez, J.A. and Goodman, D.W., *Science*, **257**, 897 (1992)
54. Hammer, B., Morikowa, Y. and Nørskov, J.K., *Phys. Rev. Lett.*, **76**, 2141 (1996)

55. Bonn, M. *et al.*, *Phys. Rev. Lett.*, **84**, 4653 (2000)
56. Shincho, E., Egawa, C., Naito, S. and Tamaru, K., *Surf. Sci.*, **149**, 1 (1985)
57. Jakob, P., *Phys. Rev. Lett.*, **77**, 4229 (1996)
58. Funk, S. *et al.*, *J. Chem. Phys.*, **112**, 9888 (2000)
59. Meyer, J.A., Schmid, P. and Behm, R.J., *Phys. Rev. Lett.*, **74**, 3864 (1995)
60. Berlowitz, P.J. *et al.*, *Surf. Sci.*, **205**, 1 (1988)
61. Hohenberg, P. and Kohn, W., *Phys. Rev.*, **136**, B864 (1964)
62. Kohn, W. and Sham, L.J., *Phys. Rev.*, **140**, A1133 (1965)
63. www.quantum-espresso.org
64. www.pwscf.org